J. Fluid Mech. (2023), *vol*. 958, A7, doi:10.1017/jfm.2023.74

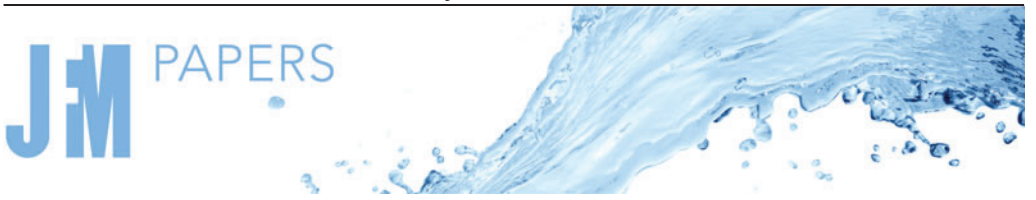

Uniform momentum and temperature zones in unstably stratified turbulent flows

Scott T. Salesky†

School of Meteorology, The University of Oklahoma, Norman, OK 73072, USA

(Received 15 July 2022; revised 21 December 2022; accepted 18 January 2023)

Wall-bounded turbulent flows exhibit a zonal arrangement, in which streamwise velocity organizes into uniform momentum zones (UMZs), separated by thin layers of elevated interfacial shear. While significant research efforts have focused on these structural features in neutrally stratified flows, the effects of unstable thermal stratification on UMZs and on analogous uniform temperature zones (UTZs) have not been considered previously. In this article, statistical properties of UMZs and UTZs are investigated using a suite of large eddy simulations of unstably stratified turbulent channel flow spanning weakly to highly convective conditions. When normalized by the friction velocity and stability-dependent mixing length, the mean velocity gradient based on UMZ interfacial velocity jumps and the vorticity thickness exhibits good collapse for all stabilities, establishing a link between UMZ properties and scaling predictions from Monin–Obukhov similarity theory. A similar relationship is found between UTZ properties and surface-layer scaling of the mean temperature gradient. In the mixed layer, mean UMZ depth is quasi-constant with wall-normal distance, while the deepest UTZs are found in the centre of the boundary layer. These instantaneous structures are found to be linked to the well-mixed velocity and temperature profiles in the convective mixed layer. Conditional averaging indicates that both UMZ and UTZ interfaces are associated with ejections of momentum and warm updrafts below the interface and sweeps of momentum and cool downdrafts above the interface. These results demonstrate a tangible connection between instantaneous structural features, mean properties and scaling laws in unstably stratified flows.

Key words: turbulent boundary layers, turbulent convection, atmospheric flows

1. Introduction

Fluid turbulence is critically important for environmental and engineering flows, regulating transport of momentum, heat and scalar quantities such as water vapour and

† Email address for correspondence: salesky@ou.edu

chemical species. Although the study of turbulence has historically been approached from a statistical perspective (e.g. Monin & Yaglom 2007*a*,*b*), numerous studies over the past several decades have revealed the importance of organized, or coherent, structures (Cantwell 1981; Robinson 1991; Panton 2001; Adrian 2007; Marusic *et al.* 2010; Jiménez 2018) in wall-bounded turbulent flows that are persistent in space and time. Structural features in wall turbulence that have been studied by investigators include low-momentum streaks (Kline *et al.* 1967; Offen & Kline 1975), hairpin vortices (e.g. Theodorsen 1952; Offen & Kline 1974; Head & Bandyopadhyay 1981; Adrian 2007), hairpin vortex packets (or large-scale motions; LSMs) (e.g. Kovasznay, Kibens & Blackwelder 1970; Brown & Thomas 1977; Adrian, Meinhart & Tomkins 2000; Ganapathisubramani, Longmire & Marusic 2003) and very large-scale motions (VLSMs) (e.g. Kim & Adrian 1999; Guala, Hommema & Adrian 2006; Balakumar & Adrian 2007; Hutchins & Marusic 2007; Marusic & Hutchins 2008). Coherent structures have received a great deal of attention, as they account for a large fraction of mass, momentum and energy transport in these flows (Corino & Brodkey 1969; Wallace, Eckelmann & Brodkey 1972; Willmarth & Lu 1972). Moreover, these organized structures are known to modulate small-scale turbulence near the wall (Mathis, Hutchins & Marusic 2009; Chung & McKeon 2010), and serve as the basis for structural models of turbulence, such as the attached eddy model (AEM), (Townsend 1976; Marusic & Monty 2019), which can accurately reproduce turbulence statistics in wall-bounded flows (Perry & Chong 1982; Perry, Henbest & Chong 1986; Perry & Marusic 1995; Woodcock & Marusic 2015).

Closely related to other coherent structures reported by investigators, Meinhart & Adrian (1995) found that instantaneous streamwise momentum in turbulent boundary layers organizes into so-called uniform momentum zones (or UMZs) characterized by nearly constant momentum, and separated by thin layers of intense interfacial shear $\partial u/\partial z$, where u is streamwise velocity and z is wall-normal distance. Meinhart & Adrian (1995) found that UMZs were prevalent in the logarithmic layer, with a streamwise length comparable to the boundary layer depth. The existence of UMZs in these flows may be viewed as a direct consequence of hairpin vortices and vortex packets. Indeed, Adrian *et al.* (2000) hypothesized that the UMZ interfaces are created by the elevated shear created by hairpin vortices; they found that these interfaces intersected the heads of individual hairpins, which are organized into packets. They also observed that a single UMZ may be associated with multiple hairpin vortex packets in the streamwise direction.

Uniform momentum zones are illustrated in figure 1, where a flow visualization is presented from an arbitrary instance of a large eddy simulation (LES; discussion to follow) of a weakly unstable convective atmospheric boundary layer ($-\delta/L = 0.3$). Here, $-\delta/L$ is a global stability parameter that can be formed from the boundary layer depth δ and the Obukhov length L. In unstably stratified flows, the Obukhov length magnitude $|L|$ can be interpreted as the wall-normal distance at which shear and buoyancy production of turbulent kinetic energy are equal (that is, shear production dominates for $z < |L|$ and buoyancy production dominates for $z > |L|$) (Wyngaard 2010). The Obukhov length is defined as

$$L = -\frac{u_\tau^3 \theta_0}{\kappa g Q_0}, \tag{1.1}$$

where $u_\tau = (-\tau_0/\rho)^{1/2}$ is the friction velocity (defined following the atmospheric boundary layer convention), $\tau_0 = \rho\,\overline{u'w'}$ is the surface shear stress (where w is the wall-normal velocity component), θ_0 is a reference potential temperature, g is gravity, κ is the von Kármán constant, $Q_0 = H_0/\rho c_p = \overline{w'\theta'}$ is the kinematic surface heat flux,

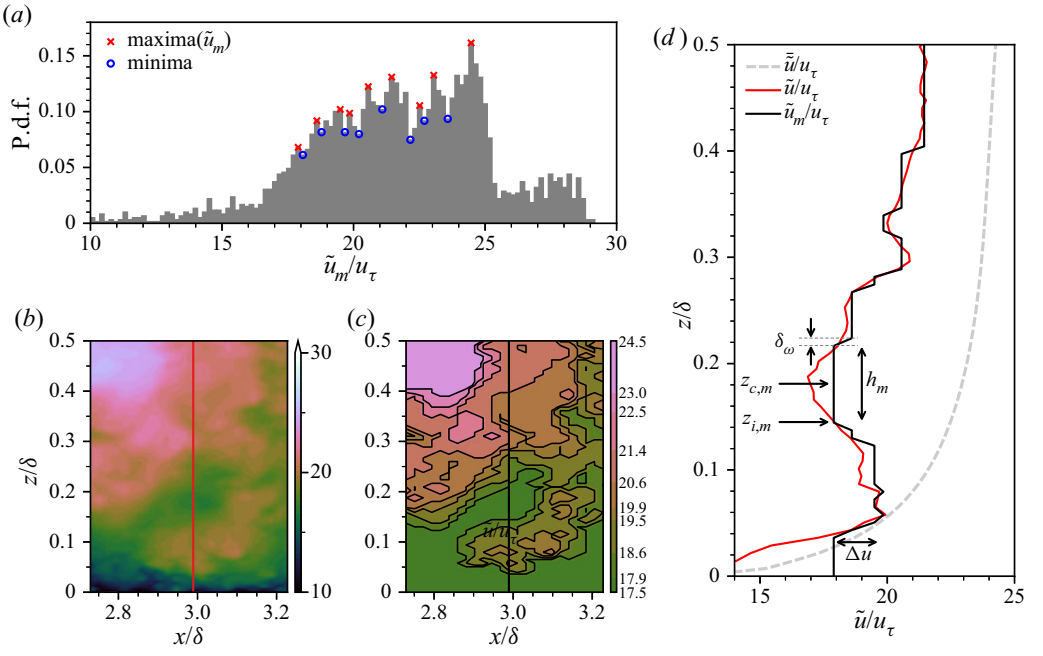

Figure 1. Example of UMZs from weakly convective LES ($-\delta/L = 0.3$). (*a*) Histogram of streamwise velocity ($\tilde{u}/u_\tau$), with detected maxima (corresponding to UMZ modal velocities) and minima (corresponding to UMZ interfaces). (*b*) Instantaneous snapshot of streamwise velocity in x–z plane. (*c*) Modal velocity ($\tilde{u}_m/u_\tau$) in each UMZ (filled contours), with UMZ interfaces denoted by black curves. (*d*) Vertical profiles (plotted for $x/\delta \approx 2.98$, denoted by vertical lines in panels *b*–*c*) of instantaneous velocity ($\tilde{u}/u_\tau$) and modal velocity ($\tilde{u}_m/u_\tau$) in each UMZ. The mean velocity ($\bar{\tilde{u}}/u_\tau$) is also displayed for comparison. Plot annotations indicate UMZ height in the wall-normal direction (h_m), velocity jump across UMZ interfaces (Δu), vorticity thickness (δ_ω), wall-normal distance to UMZ interfaces ($z_{i,m}$) and height of UMZ centroid in the wall-normal direction ($z_{c,m}$).

ρ is density, c_p is the specific heat capacity of air at constant pressure and H_0 is the surface heat flux (in W m^{-2}). The $-\delta/L \to 0$ limit corresponds to neutral stratification, whereas $-\delta/L \to +\infty$ corresponds to free convection in the absence of mean shear (analogous to Rayleigh–Bénard convection). In this work we employ a Cartesian coordinate system, where the streamwise, spanwise and wall-normal coordinates are denoted as $\boldsymbol{x} = \{x, y, z\}$ with velocity components $\boldsymbol{u} = \{u, v, w\}$. Resolved-scale quantities from LES are denoted with a tilde $\widetilde{(\cdot)}$, while an overbar $\overline{(\cdot)}$ denotes averaging in time and in horizontal planes.

An instantaneous snapshot of the resolved-scale streamwise velocity ($\tilde{u}/u_\tau$) in the x–z plane is displayed in figure 1(*b*). Uniform momentum zones, detected using a histogram-based technique (discussion to follow), are illustrated in panel (*c*), where the detected UMZ interfaces are plotted using black curves, and filled colour contours denote the modal velocity ($\tilde{u}_m/u_\tau$) within each UMZ. A histogram of streamwise velocity is displayed in panel (*a*), and includes local maxima (corresponding to modal velocities in each UMZ) and minima (corresponding to UMZ interfaces). In panel (*d*), the instantaneous velocity profile at the streamwise location $x/\delta \approx 2.98$ is plotted (red curve), along with a velocity profile composed of the modal velocity in each UMZ (black curve), and the mean velocity profile $\bar{\tilde{u}}/u_\tau$ (grey dashed curve). It is evident that the signature of UMZs in the instantaneous velocity profile is a characteristic 'stair step' pattern, with quasi-constant velocity within a given UMZ, and abrupt velocity jumps across the

UMZ interfaces. The instantaneous velocity profile can be approximated by using the modal velocity in each UMZ (black curve), which yields constant velocity in each zone and abrupt interfacial jumps. Plot annotations indicate UMZ depth in the wall-normal direction (h_m), the velocity jump across a UMZ interface (Δu), the wall-normal distance to a UMZ interface ($z_{i,m}$), the height of a UMZ centroid in the wall-normal direction ($z_{c,m}$) and the vorticity thickness (δ_ω). When ensemble averaged, these stair-step profiles give rise to the mean velocity profile; thus UMZ properties (Δu, h_m, and δ_ω) are intrinsically linked to the scaling of the mean velocity gradient $\partial\bar{u}/\partial z$ in the inertial sublayer (e.g. Heisel *et al.* 2020; Anderson & Salesky 2021; Zheng & Anderson 2022).

Investigators have found that UMZs are ubiquitous in turbulent boundary layers (Meinhart & Adrian 1995; Adrian *et al.* 2000; de Silva, Hutchins & Marusic 2016; de Silva *et al.* 2017; Laskari *et al.* 2018), channel flow (Kwon *et al.* 2014; Fan *et al.* 2019; Anderson & Salesky 2021), pipe flow (Chen, Chung & Wan 2020; Gul, Elsinga & Westerweel 2020) and the atmospheric surface layer (Morris *et al.* 2007; Heisel *et al.* 2018, 2020). de Silva *et al.* (2016) examined properties of UMZs as a function of Reynolds number ($Re_\tau = 10^3$–10^4), identifying UMZs from peaks in probability density functions (p.d.f.s) of streamwise velocity. They observed UMZs across the entire range of Re_τ considered, with the number of UMZs increasing linearly with $\log Re_\tau$. They also found that synthetic velocity fields constructed using the AEM (Townsend 1976; Perry & Chong 1982; Marusic & Monty 2019) yield similar UMZ statistics, indicating that the hierarchy of wall-attached turbulent structures present in the AEM contribute to the formation of UMZs. de Silva *et al.* (2017) considered properties of UMZ interfaces, demonstrating that sharp increases and decreases in streamwise and wall-normal velocity, respectively, occur across UMZ interfaces. Their results support the occurrence of quadrant 2 (Q2, $u' < 0$ and $w' > 0$) and quadrant 4 (Q4, $u' > 0$ and $w' < 0$) events (ejections and sweeps) below and above an interface, respectively, as one would expect if UMZ interfaces intersect the heads of hairpin vortices (Adrian *et al.* 2000; Adrian 2007).

Other investigators have reported on UMZ temporal evolution and connections to sweep and ejection events from the perspective of quadrant analysis (Laskari *et al.* 2018). This phenomenon appears to be closely related to the loading and unloading of the near-surface mean velocity gradient that has been explained in terms of the passage of LSMs aloft (Salesky & Anderson 2020*a*). Using multiple experimental and numerical data sets spanning three decades of Reynolds number, Heisel *et al.* (2020) demonstrated that in the logarithmic region of neutrally stratified flows, UMZ depth scales on distance from the wall, $h_m \sim z$, while the velocity jumps scale on the friction velocity, $\Delta u \sim u_\tau$. They interpreted interfacial shear as occurring over a layer that scales in size with the Taylor microscale (Eisma *et al.* 2015; de Silva *et al.* 2017). They thus were able to relate the scaling of the mean velocity gradient, $\partial U/\partial z \sim u_\tau/\kappa z$ to the ensemble mean of discrete velocity jumps across UMZ interfaces, and to relate the mixing length for neutral flows $\ell_m = \kappa z$ to UMZ depth, providing a physical link between scaling behaviour of the mean velocity gradient and coherent structures. A number of recent papers have also presented theoretical explanations for UMZ formation, including vortical fissure models (Chini *et al.* 2017; Bautista *et al.* 2019; Montemuro *et al.* 2020), and a bluff-body interaction model (Anderson & Salesky 2021; Zheng & Anderson 2022), where UMZ scaling properties are explained in terms of inner-layer interactions between UMZs that emanate into the outer layer.

Although they have received relatively little attention compared with UMZs, investigators have also identified uniform concentration zones (UCZs, e.g. Eisma, Westerweel & Van De Water 2021) and uniform temperature zones (UTZs, e.g. Yao *et al.*

2019; Ebadi *et al.* 2020) in wall-bounded turbulent flows with passive scalar transport or heat transfer. The UCZs and UTZs are analogous to UMZs and occur where a passive or active scalar organizes into quasi-uniform zones demarcated by large interfacial gradients. Eisma *et al.* (2021) considered UCZs in the context of point-source scalar dispersion in turbulent channel flow, noting that UCZs are closely connected to ramp-cliff structures known to form in scalar fields in turbulent shear flows (Warhaft 2000). Yao *et al.* (2019) examined UTZs in compressible turbulent channel flow for transcritical thermodynamic conditions under stable thermal stratification. They found qualitative agreement between the UMZ and UTZ interfaces, and were able to interpret their results in the context of the AEM. Ebadi *et al.* (2020) developed a one-dimensional model of heat transfer in fully developed turbulent channel flow based on the mean scalar transport equation. Their model conceptually is based on UTZs, separated by narrow regions with large interfacial gradients (so-called 'thermal fissures'). They found their model was able to reproduce profiles of the first four moments of temperature in good agreement with direct numerical simulation (DNS) results.

While a clear picture of UMZ structure and dynamics has arisen in recent years, the majority of previous work has focused on neutrally stratified flows. However, unstable thermal stratification is ubiquitous in both engineering and geophysical flows, where it is well known that buoyancy significantly modifies the mean flow, turbulence statistics and coherent structures. For example, buoyancy has significant impacts on the mean velocity and temperature profiles (Obukhov 1946; Monin & Obukhov 1954; Businger *et al.* 1971), turbulent fluxes (Wyngaard & Coté 1971; Kaimal & Finnigan 1994), integral length scales (Kaimal *et al.* 1972; Sullivan *et al.* 2003; Salesky, Katul & Chamecki 2013), turbulent kinetic energy budget (Wyngaard & Coté 1971; Frenzen & Vogel 1992, 2001), structural inclination angles (Hommema & Adrian 2003; Carper & Porté-Agel 2004; Chauhan *et al.* 2013; Salesky & Anderson 2020*b*), mean vorticity (Li & Bou-Zeid 2011; Salesky, Chamecki & Bou-Zeid 2017), partitioning between sweeps and ejections (Li & Bou-Zeid 2011; Patton *et al.* 2016; Salesky *et al.* 2017), velocity and temperature spectra (Kaimal *et al.* 1972; Kaimal & Finnigan 1994) and properties of LSMs and VLSMs (Khanna & Brasseur 1998; Salesky *et al.* 2017; Salesky & Anderson 2018). Given the impact of buoyancy on turbulence statistics and coherent structures, we anticipate that buoyancy will also have a significant impact on properties of UMZs and UTZs in unstably stratified flows.

In this paper we investigate properties of uniform momentum and temperature zones in unstably stratified turbulent channel flow – an idealized analogue of the daytime convective atmospheric boundary layer (CBL) – using a suite of LESs spanning weakly ($-\delta/L = 0.3$) to highly ($-\delta/L = 261$) unstable conditions. To the author's knowledge, the effects of unstable stratification on UMZs and UTZs have not been considered previously. The main objectives of the present study are to understand how properties of UMZs and UTZs are influenced by unstable thermal stratification and to examine the linkages between UMZ or UTZ structure, mean gradients and turbulent fluxes under unstable conditions. While the turbulent/non-turbulent interface at the CBL top also plays an important role for the dynamics of entrainment, in this present article we shall restrict our focus to internal layers (namely, UMZs and UTZs) throughout the surface layer and mixed layer of the CBL. Recall that the atmospheric surface layer (ASL) is typically defined as the lowest 10 %–15 % of the atmospheric boundary layer, where turbulent fluxes are considered to be quasi-constant with height, and Monin–Obukhov similarity theory (Obukhov 1946; Monin & Obukhov 1954) applies. In the mixed layer of the CBL, typically taken as $z/\delta \in [0.2, 0.8]$, mean values of momentum, temperature, humidity, etc. are well mixed

due to the effects of buoyancy-generated turbulence, and are quasi-constant with height (Wyngaard 2010).

When simulating a turbulent flow, one can use either DNS, where all scales of motion are resolved explicitly, or LES, where the large scales are resolved explicitly and the effects of the small scales are represented through a subgrid-scale (SGS) model. While DNS is free from modelling assumptions, it is limited to low and moderate Reynolds number flows due to its high computational expense, where the required number of grid nodes (N) increases as $N^3 \sim Re^{9/4}$ (Pope 2000); LES can resolve the production range and a portion of the inertial subrange in the bulk of the flow, but this comes at the expense of modelling assumptions in both the SGS model and wall model. In the present study, we perform wall-modelled LES, which can accurately reproduce turbulence statistics and coherent structures throughout the bulk of the convective boundary layer (e.g. Deardorff 1972; Schmidt & Schumann 1989; Moeng & Sullivan 1994; Khanna & Brasseur 1998; Sullivan & Patton 2011). In order to mitigate uncertainties associated with the LES wall model and UMZ/UTZ detection algorithm, calculated UMZ/UTZ properties (e.g. h_m, Δu, δ_ω, etc.) should be interpreted with caution in the near-wall region, i.e. $z/\delta \leqslant 0.05$ (discussion to follow).

This article is organized as follows. In §§ 2.1 and 2.2 we summarize details of the LES code and suite of simulations; the approach used to detect UMZs and UTZs is summarized in § 2.3. Results are presented in § 3, and include characterization of mean boundary layer properties (§ 3.1), number of zones as a function of stability (§ 3.2), spatial structure of UMZs and UTZs (§ 3.3), their statistical properties (§ 3.4), scaling of UMZs and UTZs in the surface layer (§ 3.5) and conditional averages of velocity and temperature relative to UMZ and UTZ interfaces (§ 3.6). Concluding remarks can be found in § 4.

2. Methodology

2.1. *Large eddy simulation code*

The LES code employed in this study is described elsewhere (e.g. Albertson & Parlange 1999; Kumar *et al.* 2006; Salesky *et al.* 2017; Salesky & Anderson 2018, 2020*b*), but code details are summarized briefly below for completeness. The LES code solves the three-dimensional filtered Navier–Stokes and potential temperature equations written in rotational form. Pseudospectral differentiation is used for horizontal derivatives, while second-order finite differences are used in the vertical. Time integration is performed using the fully explicit second-order Adams–Bashforth method, and a fractional step method (Chorin 1968; Kim & Moin 1985) is employed to compute the pressure field, using an operator-splitting technique. Full dealiasing is performed for nonlinear terms, following the 3/2 rule (Canuto *et al.* 2012). The Lagrangian scale-dependent dynamic (LASD) SGS model (Bou-Zeid, Meneveau & Parlange 2005) is used for momentum, where the optimal value of the Smagorinsky coefficient is calculated by the dynamic procedure (Germano *et al.* 1991), with averaging along Lagrangian fluid parcel trajectories (Meneveau, Lund & Cabot 1996). The SGS heat flux $q_i = \widetilde{\theta u_i} - \tilde{\theta}\,\tilde{u}_i$ is modelled assuming a constant SGS Prandtl number, i.e. $q_i = -(\nu_{sgs}/Pr_{sgs})\partial\tilde{\theta}/\partial x_i$, where $\nu_{sgs} = (c_s\Delta)^2|\tilde{S}|$ is the SGS viscosity, c_s is the Smagorinsky coefficient (determined dynamically from the LASD model for momentum) and $|\tilde{S}| = (2\tilde{S}_{ij}\tilde{S}_{ij})^{1/2}$ is the resolved-scale strain rate tensor magnitude, where $\tilde{S}_{ij} = \frac{1}{2}(\partial_j\tilde{u}_i + \partial_i\tilde{u}_j)$. The SGS Prandtl number is set to $Pr_{sgs} = 0.4$ (Kang & Meneveau 2002; Kleissl *et al.* 2006). While dynamic calculation of the SGS Prandtl number has been implemented by some investigators in LES (Porté-Agel 2004; Stoll & Porté-Agel 2006), we here use a constant SGS Prandtl number model

(with dynamic determination of c_s) in order to limit the computational expense of the simulations (Kleissl *et al.* 2006). Periodic boundary conditions are used in the horizontal directions. The upper boundary condition is stress free and zero penetration, while Monin–Obukhov similarity theory is imposed in a local sense as the lower boundary condition for momentum, with test filtering of velocity at scale 2Δ, which has been shown to better reproduce the mean surface stress (Bou-Zeid *et al.* 2005). A kinematic surface heat flux Q_0 is prescribed as the lower thermal boundary condition. A sponge layer is used in the upper 25 % of the domain following the method of Nieuwstadt *et al.* (1993) to prevent the reflection of gravity waves from the upper boundary.

2.2. *Suite of simulations*

We performed a suite of simulations similar to Salesky & Anderson (2020*b*), where we simulate turbulent half-channel flow with unstable thermal stratification and a capping inversion; the resulting flow is essentially a rotation-free convective atmospheric boundary layer. The Coriolis force was omitted from the simulations in order to simplify calculations of UMZ statistics (i.e. to eliminate the veering of the mean wind direction with height, which would unnecessarily complicate analysis of UMZ depth and interfacial velocity jumps). The initial velocity profile is imposed following Monin–Obukhov similarity theory, while for temperature we employ the three-layer profile described in Sullivan & Patton (2011) and used previously by the author (Salesky *et al.* 2017; Salesky & Anderson 2018). The initial potential temperature profile is given by

$$\bar{\theta}(z) = \begin{cases} \bar{\theta}_0, & z \leqslant \delta_0 \\ \bar{\theta}_0 + (z - \delta_0)\,\Gamma_1, & \delta_0 \leqslant z \leqslant 1.1\delta_0 \\ \bar{\theta}_0 + (z - \delta_0)\,\Gamma_1 + (z - 1.1\delta_0)\,\Gamma_2, & z \geqslant 1.1\delta_0 \end{cases}, \tag{2.1}$$

where the initial potential temperature throughout the depth of the CBL is set to $\bar{\theta}_0 = 300$ K and the inversion strengths are set to $\Gamma_1 = 0.08$ K m^{-1} and $\Gamma_2 = 0.03$ K m^{-1}. The initial boundary layer depth is set to $\delta_0 = 1000$ m; δ grows over the course of a simulation due to entrainment of fluid from the free atmosphere above the capping inversion. The boundary layer depth is defined as the height where the total (resolved + SGS) vertical heat flux, $Q = \widetilde{\tilde{w}'\tilde{\theta}'} + \bar{q}_3$, attains its minimum value (where $\bar{q}_3 = \widetilde{\widetilde{w\theta}} - \widetilde{\tilde{w}\tilde{\theta}}$). Simulations are performed over a rough wall, with the aerodynamic roughness length set to $z_0 = 0.10$ m. Because $z_0 < \Delta z$ (where Δz is the vertical LES filter width), roughness is unresolved and is represented through inclusion of z_0 in the wall model based on Monin–Obukhov similarity theory.

In the present work, we employ a domain of size $\{L_x/\delta_0, L_y/\delta_0, L_z/\delta_0\} = \{6, 6, 2\}$, with $\{N_x, N_y, N_z\} = 256^3$ grid points in the three Cartesian directions, resulting in LES filter widths of $\{\Delta x/\delta_0, \Delta y/\delta_0, \Delta z/\delta_0\} = \{2.34 \times 10^{-2}, 2.34 \times 10^{-2}, 7.81 \times 10^{-3}\}$, and a three-dimensional filter width of $\Delta/\delta_0 = 1.63 \times 10^{-2}$, where $\Delta = (\Delta x\,\Delta y\,\Delta z)^{1/3}$. Here, $\{\Delta x, \Delta y, \Delta z\} = \{L_x/N_x, L_y/N_y, L_z/N_z\}$ are LES filter widths in the x-, y- and z-directions. The domain size is sufficient to resolve LSMs but not VLSMs (Salesky & Anderson 2018) and was selected in order to enable resolution of UMZs at the highest spatial resolution reasonably attainable with our present computational resources. Grid convergence was considered previously by Salesky *et al.* (2017) with this grid spacing, but on a larger spatial domain; thus statistical quantities can be considered to be well converged for the present analysis. The simulation timestep was set to $\Delta t = 0.03$ s. Simulations were forced with a constant streamwise mean pressure gradient force $-\rho^{-1}\partial_x \bar{P}$, and an imposed

$-\rho^{-1}\partial_x\bar{P}$ (m s^{-2})	Q_0 (K m s^{-1})	δ (m)	$\lvert L\rvert$ (m)	$-\delta/L$	u_τ (m s^{-1})	$w_\star$ (m s^{-1})	w_m (m s^{-1})	$\lvert\theta_\tau\rvert$ (K)	$\lvert\theta_\star\rvert$ (K)	δ^+
1.5×10^{-3}	0.07	1082	3596	0.30	1.49	1.35	2.67	0.05	0.05	1.1×10^8
1.5×10^{-3}	0.20	1168	1470	0.79	1.56	1.96	2.88	0.13	0.10	1.2×10^8
1.1×10^{-3}	0.24	1168	661	1.8	1.27	2.06	2.67	0.19	0.12	9.9×10^7
7.0×10^{-4}	0.24	1137	258	4.4	0.93	2.06	2.34	0.26	0.12	7.1×10^7
5.0×10^{-4}	0.24	1137	124	9.2	0.73	2.06	2.20	0.33	0.12	5.5×10^7
3.0×10^{-4}	0.24	1145	41.7	27.5	0.51	2.07	2.12	0.47	0.12	3.9×10^7
1.0×10^{-4}	0.24	1145	4.4	261	0.24	2.07	2.08	1.00	0.12	1.8×10^7

Table 1. Parameters of LESs, including mean pressure gradient force ($-\rho^{-1}\partial_x\bar{P}$), kinematic surface heat flux (Q_0), boundary layer depth (δ), Obukhov length magnitude ($|L|$), global stability parameter ($-\delta/L$), shear velocity scale (u_τ), Deardorff convective velocity scale ($w_\star$), mixed velocity scale (w_m), shear temperature scale magnitude ($|\theta_\tau| = Q_0/u_\tau$), convective temperature scale magnitude ($|\theta_\star| = Q_0/w_\star$) and estimated friction Reynolds number $\delta^+ = \delta u_\tau/\nu$.

kinematic surface heat flux Q_0, which is constant in time and space. By varying these two parameters independently, it is possible to obtain a suite of simulations spanning weakly ($-\delta/L = 0.3$) to highly ($-\delta/L = 261$) convective conditions. Salient simulation parameters can be found in table 1, including the friction velocity u_τ, the Deardorff convective velocity scale $w_\star = (gQ_0\delta/\Theta_0)^{1/3}$, boundary layer depth δ and Obukhov length L. The magnitudes of both the shear and convective temperature scales, $\theta_\tau = -Q_0/u_\tau$ and $\theta_\star = -Q_0/w_\star$ respectively, along with an estimate of the friction Reynolds number $\delta^+ = \delta u_\tau/\nu$ (assuming $\nu = 1.5 \times 10^{-5}$ m^2 s^{-1}) are also reported for reference. Simulations were run for 480 000 total timesteps, equivalent to 18.0 T_ℓ for the $-\delta/L = 0.3$ case and 26.0 T_ℓ for the $\delta/L = 261$ case, where $T_\ell = \delta/w_\star$ is the large eddy turnover time.

2.3. *Detection of UMZs and UTZs*

Following previous work (Adrian *et al.* 2000; de Silva *et al.* 2016, 2017; Heisel *et al.* 2018, 2020), uniform momentum and temperature zones were identified using a histogram-based technique. When applying this technique, it is necessary to specify the spatial extent of the region of the flow to consider and the width of the bins to use when calculating histograms. The sensitivity of detected UMZ properties to these parameters has been discussed in previous work (de Silva *et al.* 2016; Laskari *et al.* 2018; Heisel *et al.* 2018). While a different choice of parameters will result in differences in calculated UMZ and UTZ properties, we emphasize that the primary focus of this study is on identifying trends in how UMZ and UTZ properties vary with stability, which are relatively insensitive to changes in the size of the streamwise window or bin width considered.

The methodology for UMZ and UTZ detection as applied to the current LES output is briefly outlined below. Instantaneous snapshots of LES in the streamwise/wall-normal plane were analysed, with streamwise and wall-normal extents $\mathcal{L}_x/\delta = 0.25$ and $\mathcal{L}_z/\delta = 1$, respectively. For each snapshot, UMZs were detected by first calculating histograms of $\tilde{u}/u_\tau$, using bins of width $0.05w_m$, where w_m is a mixed velocity scale that accounts for both buoyancy and shear (Moeng & Sullivan 1994), defined as

$$w_m = (w_\star^3 + 5u_\tau^3)^{1/3}. \tag{2.2}$$

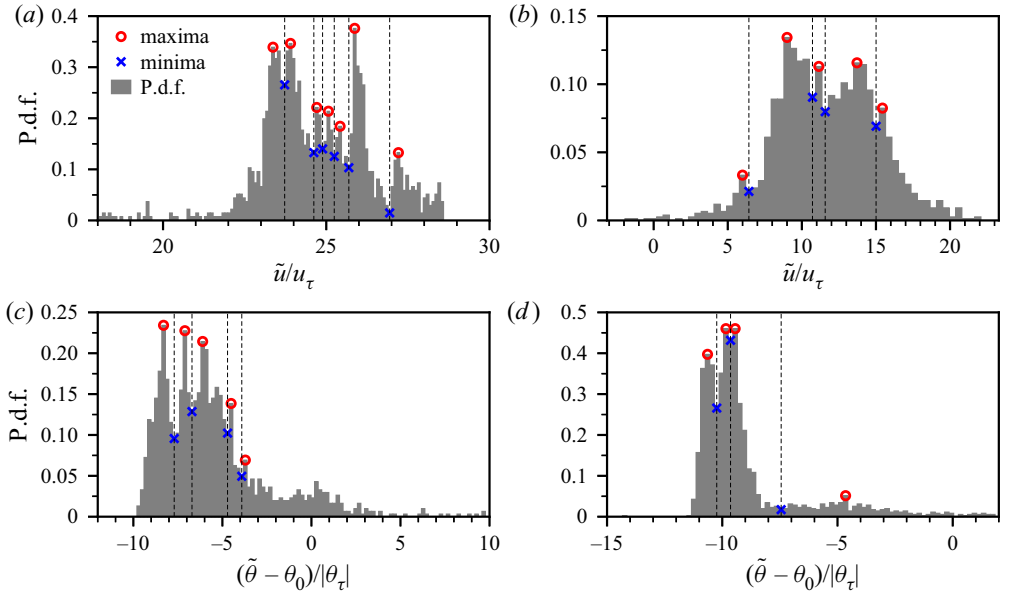

Figure 2. Example histograms of (*a*,*b*) streamwise velocity and (*c*,*d*) temperature from UMZ/UTZ detection method. Panels (*a*,*c*) are plotted for weakly convective ($-\delta/L = 0.3$) conditions, and panels (*b*,*d*) are plotted for highly convective conditions.

While the possibility of using bin widths based on u_τ alone was also considered, it was found that this led a large number of UMZs for the highly convective cases (since u_τ decreases significantly with increasing $-\delta/L$, cf. table 1), with negligible interfacial velocity jumps. On the other hand, bin widths based solely on $w_\star$ led to only 1–2 detected UMZs on average for the highly convective cases. Thus, a bin width based on w_m was employed in order so that a single bin width (in terms of w_m) could be used for all stabilities. Once histograms of $\tilde{u}/u_\tau$ were calculated, UMZs were identified from the local maxima of the histograms, subject to the criteria of (i) a minimum relative prominence of 15 % and (ii) a minimum probability of 0.01 (e.g. Heisel *et al.* 2022). The first criterion requires UMZs to have modal velocities that are 15 % larger than surrounding values, in order to ensure that neighbouring UMZs have a non-negligible contrast in momentum. The second criterion ensures that more than 1 % of the velocity values in a given instantaneous snapshot lie in a given bin for a histogram, so that infrequently occurring values of momentum are not categorized as UMZs. After identifying local maxima (which correspond to the modal velocities within each UMZ), local minima were also calculated, which are the characteristic velocities corresponding to UMZ interfaces.

An illustration of peaks detected for a single snapshot and the corresponding UMZs for an instantaneous snapshot can be found in figure 1, where panel (*a*) provides an example p.d.f. of velocity with local maxima identified (corresponding to UMZs), (*b*) is an instantaneous snapshot of streamwise velocity, (*c*) is a snapshot of modal velocities within each UMZ and UMZ interfaces and (*d*) depicts the instantaneous and mean velocity profiles. Detection of UTZs followed the same approach outlined above, except that histograms of temperature were calculated using a bin spacing of $0.2|\theta_\star| = 0.2Q_0/w_\star$ for all stabilities. Bin spacing in terms of $|\theta_\tau|$ was also considered, but θ_τ varies by a factor of $\sim$20 across all stabilities, making it challenging to find a bin width in terms of θ_τ that is appropriate for all stabilities.

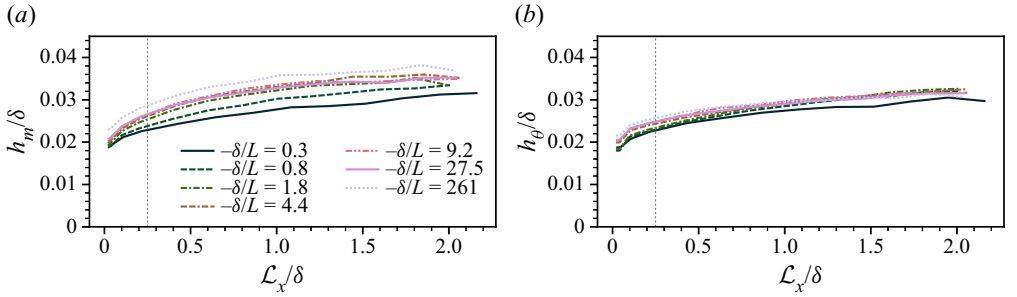

Figure 3. Average depth of uniform momentum and temperature zones in the surface layer ($z/\delta \in [0, 0.1]$) as a function of window size in the streamwise direction $\mathcal{L}_x$. (*a*) Average UMZ depth, (*b*) average UTZ depth.

Example p.d.f.s of velocity and temperature used in the UMZ/UTZ detection method are displayed in figure 2 and were calculated for arbitrary times and flow locations. Here, p.d.f.s of streamwise velocity and temperature are plotted in the upper and lower panels of figure 2, respectively, with panels (*a*,*c*) plotted for weakly unstable conditions ($-\delta/L = 0.3$) and panels (*b*,*d*) plotted for highly unstable ($-\delta/L = 261$) conditions. Red circles denote modal values of velocity/temperature in each UMZ or UTZ, while blue crosses correspond to the characteristic velocity/temperature of zone interfaces. For illustration purposes, vertical dashed lines are also plotted at velocities and temperatures corresponding to zone interfaces. One can see that bin widths become wider for more highly convective conditions, but the selected bin widths of $0.05w_m$ and $0.2|\theta_\star|$ are still sufficient for resolving multiple UMZs and UTZs in these cases (figure 2*b*,*d*).

As discussed by others (de Silva *et al.* 2016; Laskari *et al.* 2018; Heisel *et al.* 2018), properties of detected UMZs and UTZs depend on both the streamwise window extent and bin width used when calculating histograms. As the streamwise window extent $\mathcal{L}_x$ increases, local maxima in the histograms will become less distinct (eventually disappearing entirely), resulting in the detection of fewer UMZs and UTZs. Conversely, as $\mathcal{L}_x$ decreases, the limited number of points in the streamwise direction will lead to poor statistical convergence. In the present work, the streamwise window size of $\mathcal{L}_x/\delta = 0.25$ was selected in order to strike a balance between sufficient statistical convergence while still being able to resolve UMZs and UTZs. Figure 3 depicts the average depth of (*a*) UMZs and (*b*) UTZs within the surface layer as a function of $\mathcal{L}_x/\delta$. While one can see that h_m/δ and h_θ/δ are never invariant with respect to changes in $\mathcal{L}_x$, the strongest variability with $\mathcal{L}_x$ occurs for streamwise window sizes smaller than what is employed in this study. We also considered the sensitivity of UMZ and UTZ properties to the width of the bins used when calculating histograms of streamwise velocity and temperature. While increasing or decreasing the bin widths from the values $0.05w_m$ and $0.2|\theta_\star|$ employed led to slight changes in the number of UMZs and UTZs detected, the variation of UMZ and UTZ properties with changing stability ($-\delta/L$) was not particularly sensitive to the choice of bin size.

3. Results

3.1. *Mean profiles*

In order to provide broader context for UMZ- and UTZ-specific results presented in §§ 3.2–3.6, mean simulation properties are plotted as a function of dimensionless height (z/δ) and stability ($-\delta/L$) in figure 4. The convective ASL is characterized by significant positive mean wind shear and a strong negative potential temperature gradient

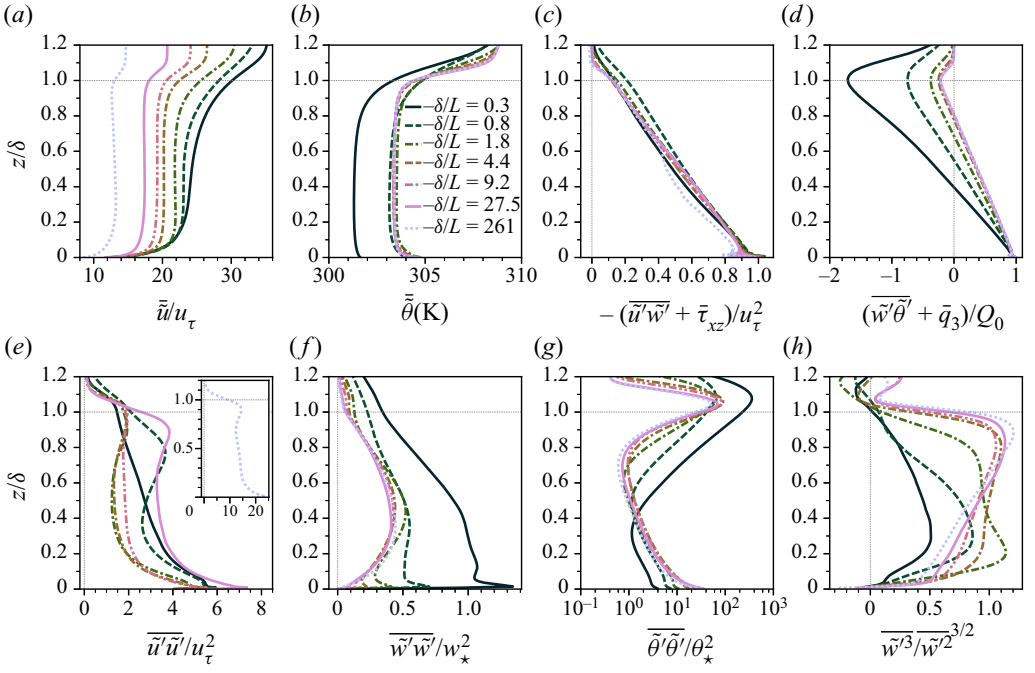

Figure 4. Mean profiles from suite of simulations as a function of dimensionless height (z/δ). (*a*) Dimensionless mean velocity profile, (*b*) mean potential temperature profile, (*c*) dimensionless kinematic momentum flux, (*d*) dimensionless kinematic heat flux, (*e*) resolved streamwise velocity variance, (*f*) resolved vertical velocity variance, (*g*) resolved potential temperature variance, (*h*) vertical velocity skewness.

figure 4(*a*,*b*), while the mean velocity and temperature profiles have negligible vertical gradients throughout the convective mixed layer (e.g. $z/\delta \in [0.2, 0.8]$). The boundary layer top (or entrainment zone) is associated with significant wind shear and a potential temperature inversion. This region of secondary shear in the entrainment zone is a well-known feature of sheared convective boundary layers (Moeng & Sullivan 1994; Conzemius & Fedorovich 2006; Fedorovich & Conzemius 2008) and occurs because surface drag reduces momentum throughout the CBL, while momentum is well mixed due to efficient buoyancy-driven vertical mixing, necessitating increased shear across the entrainment zone as the mean wind approaches its geostrophic value. The total (resolved + SGS) momentum flux (*c*) exhibits a quasi-linear profile and is similar for all stabilities, while the heat flux (*d*) decreases linearly with height until attaining negative values in the entrainment zone. Notably, both the depth of the entrainment zone (where $\overline{w'\theta'} < 0$) and the entrainment flux ratio ($-\overline{w'\theta'}_\delta/\overline{w'\theta'}_0$, where $\overline{w'\theta'}_\delta$ is the negative heat flux at the CBL top) are significantly larger for the weakly convective (i.e. shear-dominated) cases than for the more canonical (larger $-\delta/L$) cases. In the shear-free CBL, the entrainment flux ratio is typically ∼0.2 (Conzemius & Fedorovich 2006), but this can be significantly larger in sheared CBLs. Streamwise velocity variance (*e*) attains its maximum value at the surface due to the strong near-surface shear production; this is true for all stabilities. Vertical velocity variance (*f*) peaks near the ground for shear dominated cases (small $-\delta/L$) and near $z/\delta = 0.4$ for the more highly convective cases. The near-ground peak that can be observed in $\overline{w'^2}$ for weakly convective conditions occurs due to redistribution of $\overline{u'^2}$ into $\overline{v'^2}$ and $\overline{w'^2}$ through the pressure-strain covariance (e.g. Salesky *et al.* 2017).

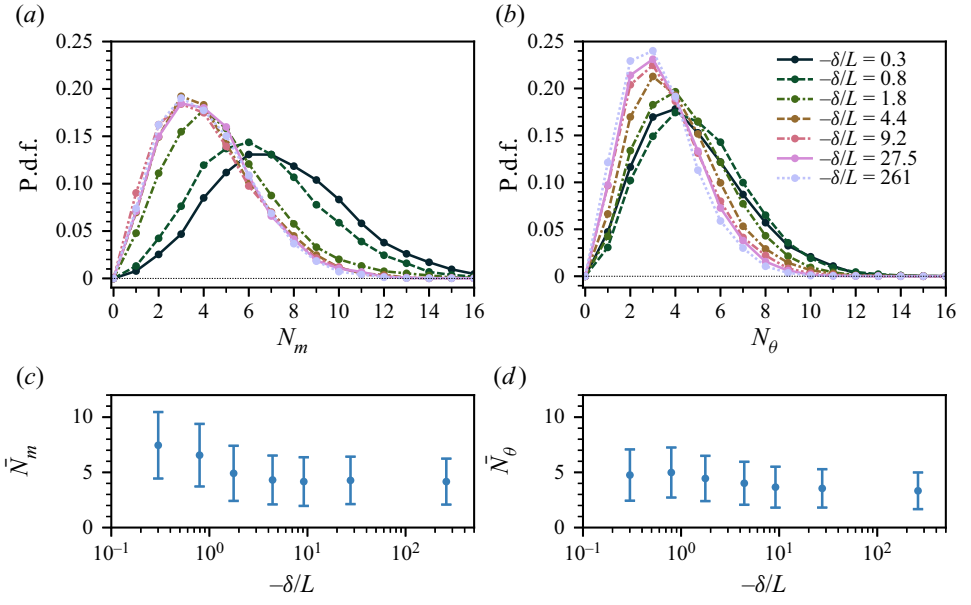

Figure 5. (*a*,*b*) Illustrate p.d.f.s of (*a*) number of UMZs (N_m) and (*b*) number of UTZs (N_θ) detected for each value of the global stability parameter ($-\delta/L$). (*c*,*d*) Indicate the mean number of (*c*) UMZs and (*d*) UTZs as a function of stability. Error bars in (*c*–*d*) are displayed for one standard deviation.

The temperature variance (g) attains its largest values near the ground and boundary layer top, and collapses well for the more convective cases ($-\delta/L \geqslant 1.8$) when normalized by $\theta_\star$. The vertical velocity skewness (h) is positive through the depth of the boundary layer for all cases considered, indicative of the intense narrow updrafts and wider but weaker downdrafts that are ubiquitous in the convective atmospheric boundary layer.

3.2. *Number of UMZs and UTZs*

We next consider how thermal stratification impacts the number of UMZs and UTZs (N_m and N_θ) present in unstably stratified flows. In figure 5, we present p.d.f.s of N_m and N_θ in panels (*a*) and (*b*) respectively; the mean number of UMZs and UTZs are plotted as a function of $-\delta/L$ in figure 5(*c*,*d*), with error bars plotted for one standard deviation. The p.d.f.s of both N_m and N_θ are positively skewed. As $-\delta/L$ increases, the medians of the N_m p.d.f.s shift to lower values, with decreasing tail probabilities. In contrast, the N_θ p.d.f.s exhibit much less sensitivity to $-\delta/L$. On average, approximately $\bar{N}_m \approx 7.5$ are found for weakly unstable conditions ($-\delta/L = 0.3$), decreasing by nearly a factor of two to $\bar{N}_m \approx 4.5$ for highly unstable ($-\delta/L = 261$) conditions (figure 5*c*). There is also a gradual decrease in the detected mean number of UTZs (*d*) from $\bar{N}_\theta \approx 4.5$ to 3.5 across the stability range considered. Thus UMZs and UTZs exhibit different responses to buoyancy forcing, with $\bar{N}_m$ decreasing as $-\delta/L$ increases, but $\bar{N}_\theta$ remaining quasi-invariant with increasing instability. Physically, this is related to the increase in inclination angle of LSMs with increasing buoyancy forcing (Hommema & Adrian 2003; Chauhan *et al.* 2013; Salesky & Anderson 2020*b*) meaning that fewer UMZs can 'fit' into the boundary layer in the wall-normal direction as unstable stratification increases. Conversely, while the spatial organization of UTZs also changes with stability, from wall-attached structures overlaid by a mixed layer to thermal plumes, both of these configurations result in a similar average

number of UTZs. Changes in the spatial structure and statistical properties of UMZs and UTZs with increasing $-\delta/L$ will be considered further below.

3.3. *Spatial structure of UMZs and UTZs*

Before turning our attention to statistical and scaling properties of UMZs and UTZs, it is instructive to first consider how the spatial structure of these zones changes with varying thermal instability. Instantaneous snapshots of velocity and temperature in the x–z plane at arbitrary times and spanwise locations are plotted in figure 6(a,c,e,g). Here, the black curves indicate UMZ or UTZ interfaces. Corresponding instantaneous velocity and temperature profiles at the locations denoted by the vertical blue lines in panels (a,c,e,g) can be found in figure 6(b,d,f,h). In each panel, the instantaneous velocity or temperature in each UMZ or UTZ is indicated by a black curve, modal values in each zone are given by the blue curves, and grey dashed curves denote ensemble mean values. Panels (a–d) correspond to near-neutral ($-\delta/L = 0.3$) conditions, while panels (e–h) correspond to highly convective ($-\delta/L = 261$) conditions. In order to illustrate the behaviour of UMZs and UTZs over a streamwise region of extent $\sim 5\delta$ (larger than the window size $\mathcal{L}_x = 0.25\delta$ used in the histogram-based detection of UMZs and UTZs), the fuzzy clustering method (FCM; Fan *et al.* 2019) was employed in figures 6–7 to calculate UMZs and UTZs. The FCM has been found to identify similar zones as the histogram-based method, given the same number of zones. We calculated the number of UMZs and UTZs in each streamwise window of size $\mathcal{L}_x = 0.25\delta$, and then mean number of zones over the entire region considered (of streamwise extent 5δ) was used input to the FCM. This is just done for illustration purposes in these figures; UMZ and UTZ statistics are calculated after zone detection using the histogram-based method discussed above.

Under weakly convective conditions (figure 6a), UMZs are organized into inclined structures increasing in depth in the downstream direction, consistent with previous findings in turbulent boundary layers (Meinhart & Adrian 1995; Adrian *et al.* 2000; de Silva *et al.* 2016). The instantaneous streamwise velocity in panel (b) exhibits the characteristic stair-step pattern reported by previous authors (de Silva *et al.* 2016, 2017; Heisel *et al.* 2020). For the near-neutral case, one UTZ is found near the ground (figure 6c), with an interface that closely corresponds to UMZ interfaces. Instantaneous temperature profiles (d) decrease with height close to the ground, and then are well mixed with only a couple of discrete UTZs present for $z/\delta \leqslant 0.8$ in this particular snapshot. However, a stair-step pattern, with large jumps in temperature can be observed in the entrainment zone (e.g. $z/\delta \geqslant 0.8$).

For highly convective conditions, UTZs encompass thermal plumes (figure 6g). However, here, the spatial structure of UMZs (panel e) is very different than that of UTZs, forming regions of alternating high and low streamwise momentum, due to horizontal convergence and divergence into the updrafts and downdrafts (e.g. Salesky *et al.* 2017). In contrast to the stair-step pattern observed in the instantaneous velocity profile for the weakly convective case, $\tilde{u}/u_\tau$ here exhibits alternating positive and negative jumps with increasing height throughout the mixed layer (figure 6f). However, the instantaneous temperature profile remains qualitatively similar to the weakly convective case. Note that negative interfacial jumps (Δu, $\Delta\theta < 0$) constitute local gradients that oppose the mean velocity and temperature gradients. Physically, the alternating positive and negative velocity and temperature jumps in the mixed layer are consistent with what is known about properties of thermal plumes in the convective mixed layer (e.g. Deardorff 1972; Schmidt & Schumann 1989; Moeng & Sullivan 1994; Khanna & Brasseur 1998). The instantaneous structure of the mixed layer is composed of both updrafts (where $w' > 0$, $\theta' > 0$, and

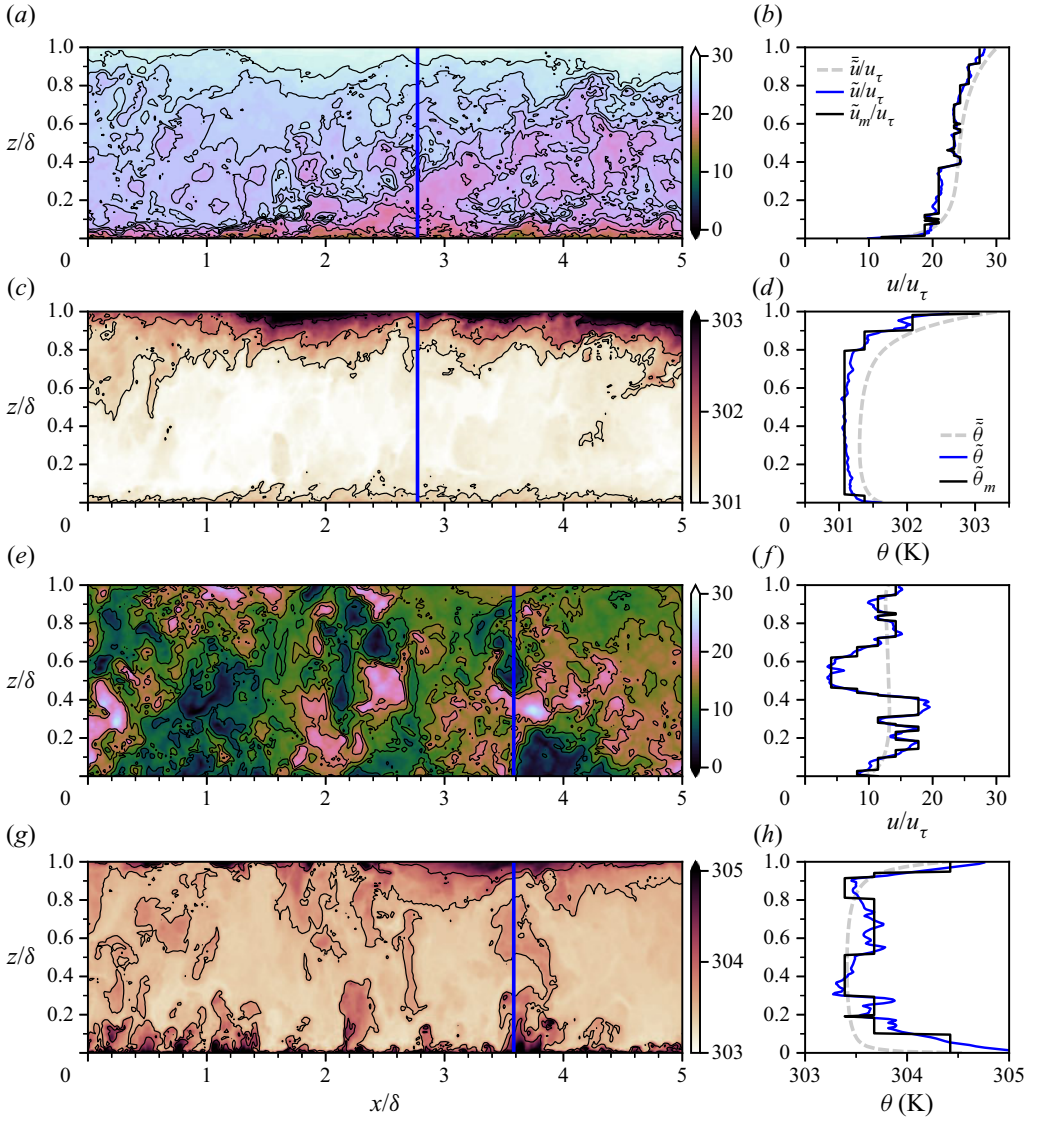

Figure 6. Examples of UMZs and UTZs from suite of simulations. (*a*,*c*,*e*,*g*) Instantaneous snapshots in x–z plane, (*b*,*d*,*f*,*h*) instantaneous profiles ($\tilde{u}/u_\tau$ and $\tilde{\theta}$), stepwise profiles based on modal velocities and temperatures in UMZs and UTZs ($\tilde{u}_m$ and $\tilde{\theta}_m$) and mean velocity and temperature ($\bar{\tilde{u}}/u_\tau$ and $\bar{\tilde{\theta}}$). Panels (*a*–*d*) are displayed for $-\delta/L = 0.30$, and (*e*–*h*) for $-\delta/L = 261$; (*a*,*b*,*e*,*f*) depict UMZs for velocity and (*c*,*d*,*g*,*h*) depict UTZs for temperature.

$u' < 0$) and downdrafts (where $w' < 0$, $\theta' < 0$, and $u' > 0$). Both updrafts and downdrafts coexist in the mixed layer, necessitating both positive and negative interfacial velocity and temperature jumps as a local and instantaneous velocity or temperature profile intersects high- and low-momentum and temperature regions. Statistical properties of these velocity and temperature jumps will be discussed further in § 3.4.

A more direct comparison between UMZ and UTZ interfaces as a function of stability can be found in figure 7. Here, streamwise velocity is plotted in the left panels and

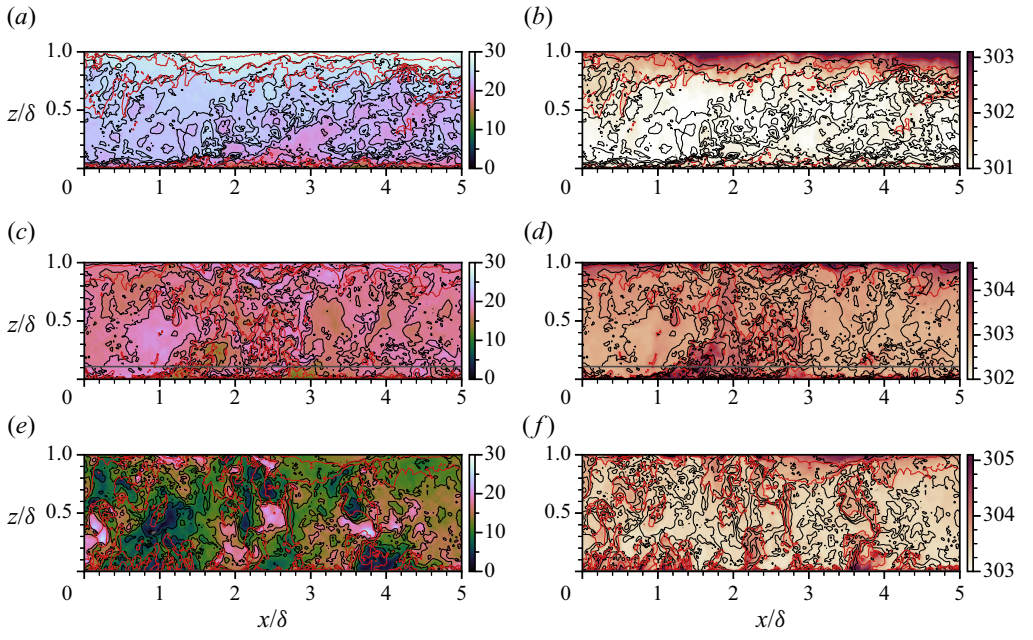

Figure 7. Comparison of UMZ and UTZ interfaces for several stabilities. Filled colour contours are plotted in the x–z plane for momentum in panels (a,c,e) and for temperature in (b,d,f). Black and red curves are used to denote UMZ and UTZ interfaces, respectively. Cases are (a,b) $-\delta/L = 0.3$, (c,d) $-\delta/L = 9.2$, (e,f) $-\delta/L = 261$. Grey horizontal lines indicate the outer-normalized Obukhov length magnitude, i.e. $-L/\delta$.

temperature in the right panels using filled colour contours, with black and red curves denoting UMZ and UTZ interfaces, respectively. Panels include flow visualizations for (a,b) $-\delta/L = 0.3$, (c,d) $-\delta/L = 9.2$, and (e,f) $-\delta/L = 261$. For the near-neutral case in panels (a,b), there is noticeable similarity between the UTZ interface detected in the surface layer (e.g. for $z/\delta \leqslant 0.1$) and the UMZ interfaces. This indicates that the coherent structures transporting momentum and heat are similar under near-neutral thermal stratification. The UMZ and UTZ interfaces are also very similar in the entrainment zone (e.g. $z/\delta \geqslant 0.8$), indicative of coinciding zones of quasi-uniform momentum and temperature. For the $-\delta/L = 9.8$ case (panels c,d), there still is similarity between the UMZ and UTZ interfaces. Here, one can see that regions of low-momentum warm fluid are being uplifted from the ground due to buoyancy. While there is not perfect agreement between UMZ and UTZ interfaces, some corresponding features can be observed in both the streamwise momentum and temperature fields. For the most highly convective case ($-\delta/L = 261$, panels e,f), there is a marked difference between the UMZ and UTZ interfaces. As buoyancy forcing increases, the horizontal momentum field is driven primarily by convergence and divergence into and out of buoyant updrafts and downdrafts. Here, warm updrafts are flanked by high- and low-momentum fluid, such that momentum and temperature are out of phase. Thus, under highly convective conditions, the UMZ interfaces deviate from the UTZ interfaces that encompass thermal plumes.

The results presented in figure 7 are consistent with previous findings in the convective boundary layer literature (Li & Bou-Zeid 2011; Patton *et al.* 2016; Salesky *et al.* 2017), which have demonstrated a breakdown of Reynolds' analogy – the assumption that momentum and scalars are transported similarly by turbulence – as $-\delta/L$ increases. Using *in situ* ASL observations, Li & Bou-Zeid (2011) found significant differences between

the momentum flux ($\overline{u'w'}$) and heat flux ($\overline{w'\theta'}$) in the CBL with increasing instability. They hypothesized that these differences were due a transition in coherent structures from hairpin vortices to thermal plumes. A subsequent LES study by Salesky *et al.* (2017) found an order of magnitude decrease in the momentum transport efficiency (the downgradient fraction of the total flux) in the ASL, while the heat transport efficiency only varied by 10 % from weakly to highly convective conditions. They also observed – in support of the hypothesis of Li & Bou-Zeid (2011) – a concurrent decrease in spanwise vorticity and increase in vertical vorticity with increasing $-\delta/L$, as one would expect if there was a transition from hairpin vortices to vertically dominant thermal plumes. This breakdown of Reynolds analogy with increasing instability can be interpreted in the context of the spatial differences between UMZs and UTZs that are observed in figure 7. Under weakly convective conditions, the UMZ interfaces – which intersect heads of hairpin vortices (Adrian *et al.* 2000) – and UTZ interfaces are collocated, such that hairpin vortex packets transport momentum and heat in a similar manner. However, as $-\delta/L$ increases, the UTZ interfaces encompass thermal plumes while UMZ organization becomes increasingly influenced by convergence and divergence from updrafts and downdrafts. Thus, distinctly different structural features are found in the streamwise momentum and temperature fields as buoyancy forcing increases, leading to the breakdown of Reynolds' analogy with increasing $-\delta/L$.

3.4. *The UMZ and UTZ statistics*

In this section we consider how statistical properties of UMZs and UTZs, including the interfacial velocity and temperature jumps and the depth of the zones, vary with unstable stratification. The UMZs and UTZs were detected using a histogram-based method (discussed in § 2.3), then a stepwise profile was constructed using the modal velocity or temperature in each zone corresponding to the detected local maxima (figure 1 schematic). The modal velocity profile was used to determine mean UMZ depth (h_m) in the wall-normal direction, which was assigned to the height of the UMZ centre $z_{c,m}$ illustrated in figure 1(*c*). The interfacial velocity jumps were assigned to the wall-normal height of the UMZ interface $z_{i,m}$. This was done for each instantaneous profile, and statistics were calculated by averaging in time and in horizontal planes to obtain vertical profiles of h_m and Δu as a function of z/δ. An analogous procedure was used to calculate UTZ statistics. The interfacial velocity and temperature jumps (Δu and $\Delta\theta$) are defined as the difference in the modal velocities (corresponding to the local maxima in histograms) between subsequent UMZs or UTZs.

The mean depths of UMZs and UTZs and the mean interfacial velocity and temperature jumps are displayed in figure 8. The UMZ depth h_m is plotted as a function of z/δ in panels (*a*,*b*) and UTZ depth h_θ is plotted in panels (*d*,*e*), where the depth of the zones is normalized by the outer length scale δ in the first column and by height z in the second column. Panels in the right column depict the (*c*) mean velocity jumps across UMZ interfaces and (*d*) mean temperature jumps across UTZ interfaces.

Near the ground, the average depth of both UMZs and UTZs is $\approx 2z$ (figure 8*b*,*e*). This is consistent with the attached eddy hypothesis (Townsend 1976), which states that the vertical extent of turbulent eddies is regulated by their distance from the wall. However, some caution in interpretation is warranted here, given the influence of the LES wall model on near-wall statistics and uncertainties in the UMZ/UTZ detection technique near the wall. Note that zones are not typically identified for low values of $\tilde{u}/u_\tau$ (e.g. figures 1–2), as these zones do not satisfy all the detection criteria. Future studies using DNS or

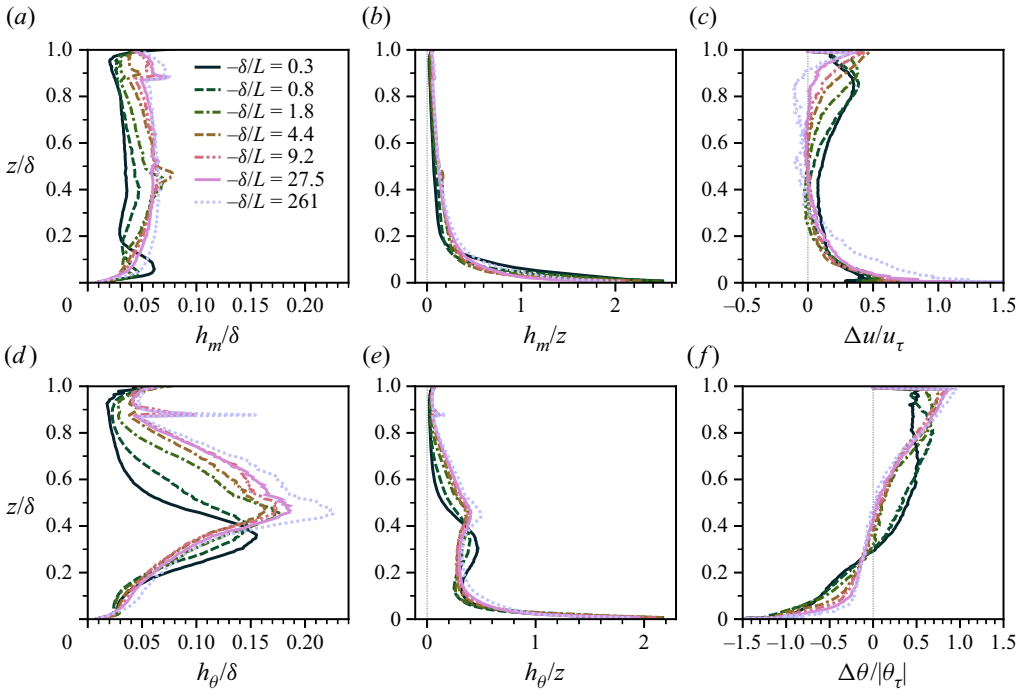

Figure 8. Vertical profiles of mean UMZ and UTZ properties. (*a*) Average depth of UMZs (h_m), normalized by boundary layer depth δ, (*b*) average depth of UMZs normalized by height z, (*c*) average velocity jump (Δu) across UMZ interfaces normalized by shear velocity scale u_τ, (*d*) average depth of UTZs (h_θ) normalized by boundary layer depth δ, (*e*) average depth of UTZs normalized by height z, (*f*) average temperature jump across UTZ interfaces normalized by shear temperature scale magnitude $|\theta_\tau|$.

wall-resolved LES to study near-wall properties of UMZs and UTZs in unstably stratified flows are therefore needed.

The outer-normalized UMZ depth (panel *a*) is quasi-constant throughout the mixed layer for all stabilities considered, with h_m/δ increasing with increasing $-\delta/L$. This relative invariance with height points to similar physical mechanisms being responsible for UMZ generation throughout the mixed layer across the stabilities considered here. Near the ground, the average jump in velocity across UMZ interfaces is $\Delta u \approx 0.5$–$1.0u_\tau$. In the mixed layer, the velocity jumps are very small ($\Delta u \approx 0.2u_\tau$) for the near-neutral case, and are near zero for the more highly convective cases. In the entrainment zone (e.g. $z/\delta \geqslant 0.8$), the velocity jumps again increase to values of $\Delta u \approx 0.4$–$0.5u_\tau$, due to the region of secondary mean wind shear that is a ubiquitous feature of sheared convective boundary layers (e.g. figure 4*a*).

For the weakly convective cases ($-\delta/L = 0.3, 0.8$) the mean UTZ depth (figure 8*d*,*e*) attains its maximum value near $z/\delta = 0.3$–0.4, corresponding to deeper UTZs in the mixed layer. This is consistent with the instantaneous structure of UTZs which can be seen in the flow visualizations in figure 6. Similar behaviour is observed for the more convective cases, except with both maximum zone depth ($h_\theta/\delta \approx 0.2$) and the height of maximum zone depth increasing with $-\delta/L$. For all stabilities, $\Delta\theta$ is negative in the surface layer, and changes sign around $z/\delta \approx 0.3$ for the weakly convective cases and around $z/\delta \approx 0.5$ for the highly convective cases. The height at which $\Delta\theta/|\theta_\tau|$ changes sign is comparable to the lower boundary of the entrainment zone where $\overline{w'\theta'}$ becomes negative (e.g. figure 4*d*).

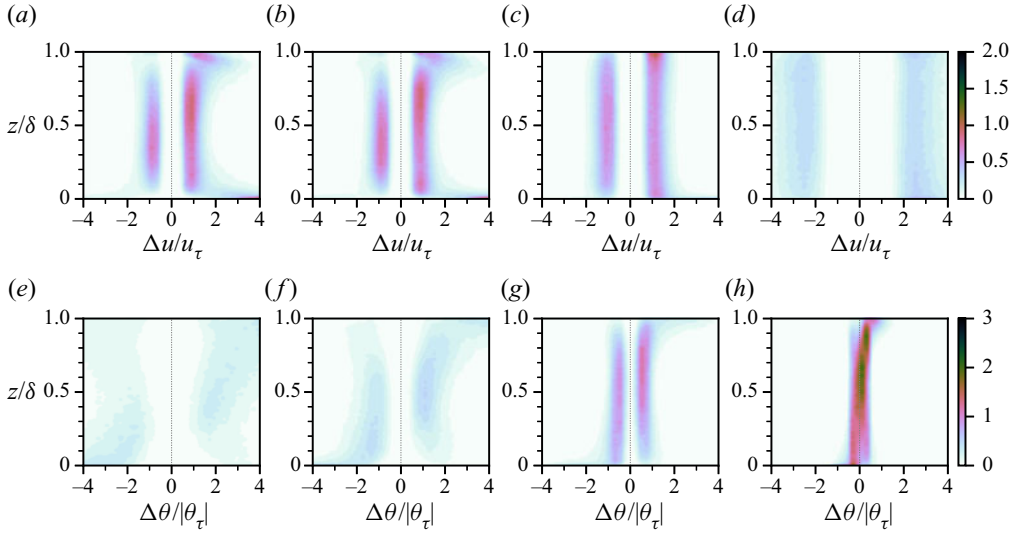

Figure 9. Probability density functions of UMZ and UTZ properties as a function of dimensionless height (z/δ). (*a–d*) Dimensionless velocity jump across UMZ interfaces ($\Delta u/u_\tau$), (*e–h*) dimensionless temperature jump across UTZ interfaces ($\Delta\theta/|\theta_\tau|$); (*a*,*e*) $-\delta/L = 0.3$, (*b*,*f*) $-\delta/L = 0.79$, (*c*,*g*) $-\delta/L = 9.2$, (*d*,*h*) $-\delta/L = 261$.

In addition to characterizing mean properties of UMZs and UTZs, it is also useful to consider the distributions of interfacial velocity and temperature jumps. In figure 9, p.d.f.s are presented of (*a–d*) UMZ interfacial velocity jumps and (*e–h*) UTZ interfacial temperature jumps. Here, the abscissa corresponds to the normalized variable of interest, the ordinate axis to dimensionless height (z/δ), and filled colour contours to values of the p.d.f. Several selected stabilities are displayed, specifically $-\delta/L = 0.3$, 0.8, 9.2 and 261 in the columns from left to right.

For all stabilities considered here, the most probable interfacial velocity jumps in the surface layer and entrainment zone are positive. However, in the mixed layer, the p.d.f.s of $\Delta u/u_\tau$ exhibit bimodal behaviour, which is consistent with the alternating positive and negative $\Delta u/u_\tau$ observed from the flow visualizations in figure 6. For the more weakly convective cases ($-\delta/L = 0.3, 0.79, 9.2$), the most probable values of velocity jumps in the mixed layer are $\Delta u \approx \pm 1.0 u_\tau$. The magnitude of the mixed layer velocity jumps increases to $|\Delta u| \approx 2.5 u_\tau$ for the most convective ($-\delta/L = 261$) case. The p.d.f.s of interfacial temperature jumps are consistent with the mean profiles (figure 8*f*) where the most probable value of $\Delta\theta$ is negative near the surface, positive in the entrainment zone, and exhibits bimodal behaviour in the mixed layer – indicative of alternating positive and negative jumps. The magnitude of the interfacial temperature jumps in the mixed layer decreases with increasingly unstable conditions, from $|\Delta\theta| \approx 2|\theta_\tau|$ for $-\delta/L = 0.3$ to $|\Delta\theta| \approx 0.5|\theta_\tau|$ for $-\delta/L = 261$.

To summarize, we find that in the surface layer, the average depth of UMZs and UTZs is $\approx 2z$, consistent with the attached eddy hypothesis, although these results should be interpreted with some caution given the influence of the LES wall model. In the mixed layer, the depth of UMZs approach constant values for a given stability, ranging from $h_m/\delta = 0.03$–0.06, and increasing with $-\delta/L$. The UTZ depth is at is maximum in the centre of the boundary layer, attaining values of $h_\theta = 0.15\delta$ to 0.23δ, indicating of a deep zone of quasi-uniform temperature typically present in the centre of the

mixed layer. Interfacial velocity jumps are largest in the surface layer and the entrainment zone, and become quite small (e.g. $|\Delta u| < 0.2u_\tau$) throughout the mixed layer. Interfacial temperature jumps are negative near the ground, positive in the entrainment zone, and change sign at a height that roughly corresponds to the bottom of the entrainment zone (where $\overline{w'\theta'}$ becomes negative. The surface-layer scaling of UMZ and UTZ properties will be considered further in the following section.

3.5. *The UMZs, UTZs and scaling laws in the surface layer*

We now consider the extent to which UMZ and UTZ properties in the ASL can explain scaling laws for the dimensionless mean velocity and temperature gradients under unstably stratified conditions. A recent paper (Heisel *et al.* 2020) argued that under neutral stratification, UMZs can be linked to the hypothetical turbulent eddies that Prandtl (1925) invoked in his derivation of the logarithmic law of the wall. Following Prandtl's arguments, the mean velocity gradient can be written as

$$\frac{\partial \bar{U}}{\partial z} \sim \frac{u_\tau}{\ell_m}. \tag{3.1}$$

Here, ℓ_m is the mixing length, which can be interpreted as the characteristic length scale over which turbulent eddies transport momentum. Assuming $\ell_m = \kappa z$ under neutral stratification, (3.1) can be integrated to obtain the log law

$$\frac{\bar{U}}{u_\tau} = \frac{1}{\kappa} \ln z^+ + A_u, \quad z^+ = \frac{z u_\tau}{\nu}, \tag{3.2a,b}$$

where A_u is a constant that depends on the surface roughness.

Heisel *et al.* (2020) related the scaling of the mean velocity gradient in the inertial sublayer to UMZ properties

$$\frac{\partial \bar{U}}{\partial z} = \frac{u_\tau}{\kappa z} \sim \frac{\Delta u}{h_m}, \tag{3.3}$$

where they envisioned the mean gradient as arising due to the collective effects of an ensemble of interfacial velocity jumps (Δu) over zones of depth h_m. They presented evidence that under neutral stratification the interfacial velocity jumps scale on the friction velocity, $\Delta u \sim u_\tau$, while UMZ depth scales on the neutral mixing length $h_m \sim \ell_m = \kappa z$. In this manner, they linked coherent structures in the flow (i.e. UMZs associated with mean shear) to the log law.

Other authors (Anderson & Salesky 2021; Zheng & Anderson 2022) have instead suggested that the salient length scale linking UMZs to the mean velocity gradient is the vorticity thickness δ_ω (Brown & Roshko 1974; Chauhan *et al.* 2014; de Silva *et al.* 2017; Bautista *et al.* 2019), defined as

$$\delta_\omega = \frac{|\Delta u|}{\max|\partial \langle U \rangle / \partial z|}, \tag{3.4}$$

where $\langle \cdot \rangle$ denotes a conditional average across a UMZ interface. On physical grounds, this corresponds to shear being concentrated in thin regions of thickness δ_ω associated with UMZ interfaces, and negligible shear within each zone. Note that absolute values are used

in (3.4) so that δ_ω is non-negative by definition. From this perspective, one would expect the mean gradient to scale as

$$\frac{\partial \bar{U}}{\partial z} = \frac{u_\tau}{\ell_m} \sim \frac{\Delta u}{\delta_\omega}. \tag{3.5}$$

One can also invoke mixing length arguments to derive a surface-layer scaling for the mean temperature gradient, by hypothesizing that the mean temperature gradient scales as the ratio of a shear temperature scale θ_τ to the mixing length for heat ℓ_h

$$\frac{\partial \bar{\theta}}{\partial z} = \frac{\theta_\tau}{\ell_h}. \tag{3.6}$$

Using the neutral mixing length $\ell_h = \kappa z$, one can integrate (3.6) to show that, under near-neutral stratification, the mean temperature profile also follows a log law

$$\frac{\bar{\theta} - \theta_s}{\theta_\tau} = \frac{1}{\kappa} \ln z^+ + A_\theta, \tag{3.7}$$

where θ_s is surface temperature, and A_θ is a constant that depends on the surface roughness. From the perspective of UTZs, the equivalent statement to (3.5) is

$$\frac{\partial \bar{\theta}}{\partial z} = \frac{\theta_\tau}{\ell_h} \sim \frac{\Delta \theta}{\delta_{\nabla\theta}}. \tag{3.8}$$

That is, one may hypothesize that the mean surface-layer temperature gradient arises due to the ensemble effects of interfacial temperature jumps $\Delta\theta$ across UTZ interfaces of thickness $\delta_{\nabla\theta}$ and negligible gradients within each UTZ. Through analogy with δ_ω, one may define a temperature gradient thickness $\delta_{\nabla\theta}$

$$\delta_{\nabla\theta} = \frac{|\Delta\theta|}{\max|\partial\langle\theta\rangle/\partial z|}. \tag{3.9}$$

Under thermally stratified conditions, the mean velocity profile (MVP) in the surface layer deviates from the log law due to buoyancy effects. The effects of thermal stratification on the MVP and other turbulence statistics in the ASL can be explained in the context of Monin–Obukhov similarity theory (MOST; Obukhov 1946; Monin & Obukhov 1954), where any turbulence statistic non-dimensionalized using the height z, friction velocity u_τ and buoyancy parameter g/Θ_0 and the kinematic surface heat flux Q_0 is predicted to be a universal function of the Monin–Obukhov stability variable $\zeta = z/L$. Here, L is the Obukhov length given in (1.1). Thus, under thermally stratified conditions, the dimensionless mean velocity and temperature gradients are predicted be universal functions of ζ

$$\frac{\kappa z}{u_\tau}\frac{\partial \bar{U}}{\partial z} = \phi_m(\zeta), \tag{3.10}$$

$$\frac{\kappa z}{\theta_\tau}\frac{\partial \bar{\theta}}{\partial z} = \phi_h(\zeta). \tag{3.11}$$

The universal functions $\phi_m(\zeta)$ and $\phi_h(\zeta)$ must be determined empirically; many formulations are available in the literature (e.g. Businger *et al.* 1971; Högström 1988; Brutsaert 1999). In this article, we use the empirical functions for ϕ_m and ϕ_h presented by Brutsaert (1999) based on the directional dimensional analysis of Kader & Yaglom

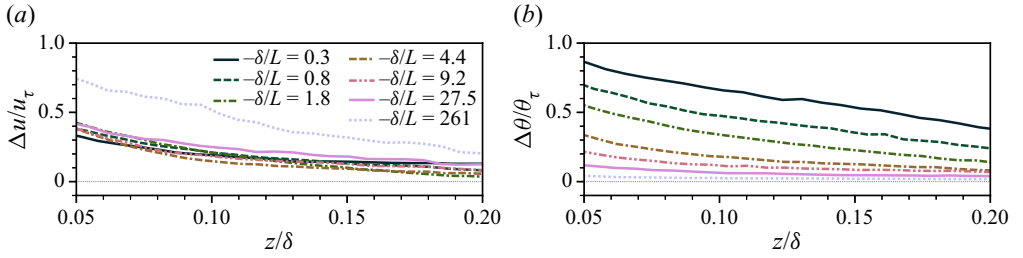

Figure 10. Velocity and temperature jumps across UMZ and UTZ interfaces, respectively, in the surface layer. (*a*) Interfacial velocity jumps Δu, normalized by shear velocity scale u_τ, (*b*) interfacial temperature jumps $\Delta\theta$, normalized by shear temperature scale θ_τ.

(1990). These empirical functions are used because they capture the local free convective scalings $\phi_m(\zeta) \propto (-\zeta)^{1/3}$ and $\phi_h(\zeta) \propto (-\zeta)^{-1/3}$ for $-\zeta \gg 1$; additional details can be found in Appendix A.

Following MOST, the mean velocity and temperature gradients under thermally stratified conditions are given as

$$\frac{\partial \bar{U}}{\partial z} = \frac{u_\tau}{\ell_m} = \frac{u_\tau}{\kappa z/\phi_m(\zeta)} \tag{3.12}$$

and

$$\frac{\partial \bar{\theta}}{\partial z} = \frac{\theta_\tau}{\ell_h} = \frac{\theta_\tau}{\kappa z/\phi_h(\zeta)}. \tag{3.13}$$

In (3.12)–(3.13), ℓ_m and ℓ_h are the stability dependent mixing lengths for momentum and temperature, defined as

$$\ell_m = \frac{\kappa z}{\phi_m(\zeta)} \tag{3.14}$$

$$\ell_h = \frac{\kappa z}{\phi_h(\zeta)}. \tag{3.15}$$

Because $\phi_m(\zeta) < 1$ and $\phi_h(\zeta) < 1$ for unstable conditions, the mixing lengths under unstable stratification exceed their neutral values ($\ell_m > \kappa z$ and $\ell_h > \kappa z$ for $\zeta < 0$), which physically corresponds to enhanced mixing due to the effects of buoyancy-generated turbulence under unstable thermal stratification.

Before examining the linkages between UMZ and UTZ properties and the scaling of the mean velocity and temperature gradients in the atmospheric surface layer following MOST, we first shall consider the surface layer behaviour of the relevant velocity and temperature scales (Δu and $\Delta\theta$) and length scales (h_m, h_θ, δ_ω and $\delta_{\nabla\theta}$). The shear-normalized interfacial velocity and temperature jumps in the surface layer are displayed in figure 10(*a*,*b*). Here, Δu and $\Delta\theta$ are only displayed for $z/\delta \geqslant 0.05$ given uncertainty in zone detection and the influence of the LES wall model close to the surface. One can see that when normalized by u_τ, the interfacial velocity jumps in the surface layer (figure 10*a*) collapse reasonably well to a single curve for all stabilities except for the most convective case ($-\delta/L = 261$). However, the interfacial temperature jumps, displayed in panel (*b*) do not collapse, but rather exhibit a systematic ordering where $\Delta\theta/\theta_\tau$ decreases monotonically with increasing $-\delta/L$ for a given value of z/δ. Both Δu and $\Delta\theta$ decrease with increasing distance from the ground, consistent with previous studies (e.g. de Silva *et al.* 2017; Heisel *et al.* 2020).

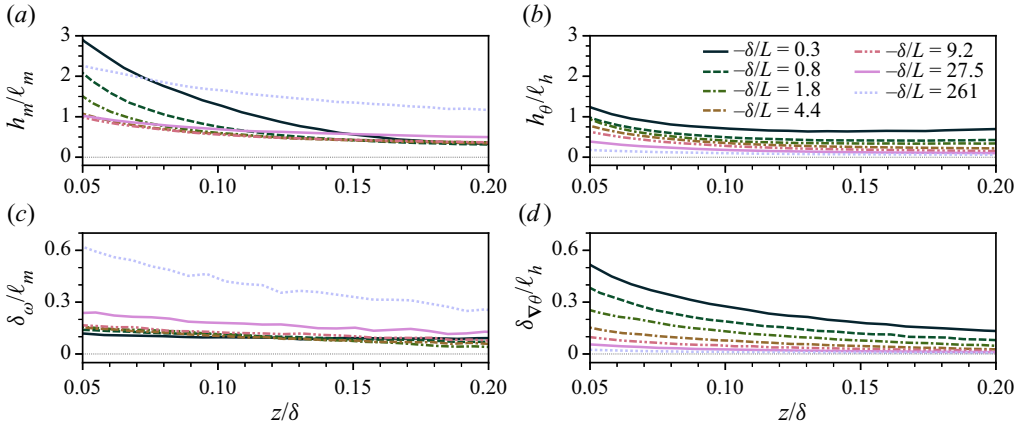

Figure 11. Behaviour of length scales associated with UMZs and UTZs in the surface layer; (*a*) UMZ depth h_m, (*b*) UTZ depth h_θ, (*c*) vorticity thickness δ_ω, (*d*) temperature gradient thickness $\delta_{\nabla\theta}$. Length scales are normalized by the mixing lengths for momentum $\ell_m = \kappa z/\phi_m(\zeta)$ and heat $\ell_h = \kappa z/\phi_h(\zeta)$.

Surface-layer behaviour of the length scales associated with UMZs and UTZs is illustrated in figure 11, with the panels corresponding to (*a*) UMZ depth h_m, (*b*) UTZ depth h_θ, (*c*) vorticity thickness δ_ω and (*d*) temperature gradient thickness $\delta_{\nabla\theta}$. These length scales associated with UMZs and UTZs are normalized by the stability-dependent mixing lengths for momentum ℓ_m, and heat ℓ_h, respectively (3.14)–(3.15). One can see that the curves for different $-\delta/L$ values for h_m/ℓ_m begin to collapse above $z/\delta = 0.15$, but exhibit a significant amount of spread closer to the ground. The normalized vorticity thickness (panel *c*) exhibits better collapse than the UMZ depth for all heights displayed here, except for the most unstable cases ($-\delta/L = 27.5, 261$), indicating that it is a more appropriate mixing length for momentum than h_m in the surface layer under unstable stratification. Length scales associated with UTZs are displayed in the right panels of figure 11, with UTZ depth in panel (*b*) and temperature gradient thickness in panel (*d*). One can see that neither h_θ or $\delta_{\nabla\theta}$ collapse to a single curve when normalized by ℓ_h, and both decrease systematically with increasing $-\delta/L$. However, this $-\delta/L$ dependence is comparable to what is found for $\Delta\theta/\theta_\tau$ (figure 10*b*), suggesting that collapse of the normalized gradients still may be possible.

The connection between the mean velocity and temperature gradients in the surface layer and properties of UMZs and UTZs is examined in figure 12. The left panels depict the extent to which the scaling of the surface-layer mean velocity gradient following MOST is related to UMZ properties, with panel (*a*) considering the scaling $\partial\bar{U}/\partial z \sim \Delta u/h_m$ and panel (*b*) considering the scaling $\partial\bar{U}/\partial z \sim \Delta u/\delta_\omega$. In both panels, the gradients based on UMZ properties are normalized by ℓ_m/u_τ. If a scaling is appropriate, one would expect collapse of all curves for different stabilities ($-\delta/L$ values) to an $O(1)$ constant. One can see that both scalings for $\partial\bar{U}/\partial z$ lead to reasonably good collapse of all curves in panels (*a*,*c*). The normalized velocity gradient calculated using δ_ω as the length scale in figure 12(*c*) does exhibit some weak $-\delta/L$ dependence. Note that previous observational and LES studies have found that calculated values of ϕ_m exhibit significant scatter and do not collapse as a function of ζ alone (Khanna & Brasseur 1997; Johansson *et al.* 2001; Salesky & Chamecki 2012). These deviations from Monin–Obukhov similarity have been explained by taking $-\delta/L$ as an additional scaling parameter (Khanna & Brasseur 1997; Johansson *et al.* 2001) and by accounting for the large-scale velocity due to LSMs in

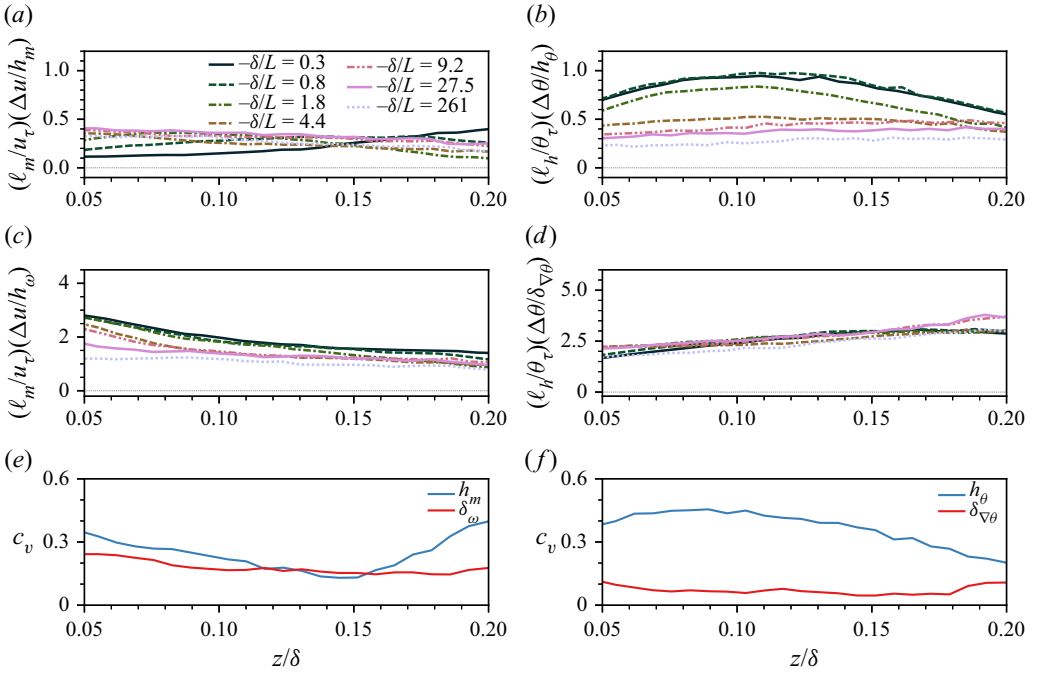

Figure 12. Surface-layer scaling of mean velocity and temperature gradients based on UMZ and UTZ properties. (*a*) Mean velocity gradient based on interfacial velocity jumps and UMZ depth $\Delta u/h_m$. (*b*) Mean temperature gradient based on interfacial temperature jumps and UTZ depth $\Delta\theta/h_\theta$. (*c*) Mean velocity gradient based on interfacial velocity jumps and vorticity thickness $\Delta u/\delta_\omega$. (*d*) Mean temperature gradient based on interfacial temperature jumps and temperature gradient thickness $\Delta\theta/\delta_{\nabla\theta}$. Mean gradients are normalized by shear velocity and temperature scales (u_τ and θ_τ), and stability-dependent mixing lengths for momentum and heat (ℓ_m and ℓ_h). Panels (*e–f*) include the coefficients of variation (3.16) for the curves in panels (*a–d*), indicative of the level of collapse to a single curve for the different scalings.

dimensional analysis (Salesky & Anderson 2020*a*). The amount of scatter in scalings based on h_m and δ_ω can be quantified by considering the coefficient of variation c_v, defined as

$$c_v = \frac{\sigma(z/\delta)}{\mu(z/\delta)}, \tag{3.16}$$

that is, the ratio of the standard deviation to mean of the normalized gradients, where both μ and σ are taken across the seven different $-\delta/L$ values considered here. Smaller values of c_v indicate better collapse to a single curve (i.e. less scatter). One can see from figure 12(*e*) that while using h_m or δ_ω yield similar values of c_v at some heights, overall employing δ_ω as a length scale leads to better collapse of the normalized mean velocity gradient on average throughout the ASL.

Surface-layer scaling of the mean temperature gradient based on UTZ properties is considered in the right panels of figure 12, with normalization based on UTZ depth in panel (*b*), normalization based on temperature gradient thickness in (*d*) and profiles of c_v in (*f*). One can see that the scaling based on UTZ depth ($\partial\bar{\theta}/\partial z \sim \Delta\theta/h_\theta$), considered in panel (*b*) exhibits significantly more scatter than the scaling based on temperature gradient thickness ($\partial\bar{\theta}/\partial z \sim \Delta\theta/\delta_{\nabla\theta}$) in panel (*d*). This is further supported by the coefficient of variation profiles in panel (*f*). Physically, this indicates that the temperature gradient thickness $\delta_{\nabla\theta}$ is a more appropriate mixing length for temperature than h_θ, which

is consistent of the picture of gradients being predominately concentrated across UTZ interfaces and occurring over length $\delta_{\nabla\theta}$.

While scalings for the surface-layer mean velocity and temperature gradients $\partial\bar{U}/\partial z \sim \Delta u/\delta_\omega$ and $\partial\bar{\theta}/\partial z \sim \Delta\theta/\delta_{\nabla\theta}$ exhibit reasonable collapse to a single curve for all stabilities when normalized by the mixing lengths (ℓ_m and ℓ_h), and shear velocity and temperature scales (u_τ and θ_τ), there is still a weak z/δ dependence observed within the surface layer. While the empirical Businger–Dyer curves (Dyer 1974) also were considered (which follow $\phi_m \propto (-\zeta)^{-1/4}$ and $\phi_h \propto (-\zeta)^{-1/2}$ scaling behaviour for weakly convective conditions), we found that the empirical MOST functions from Brutsaert (1999) (based on Kader & Yaglom 1990) lead to superior collapse of the normalized gradients. Evidently, it is important to account for local free convective scaling ($\phi_m \propto (-\zeta)^{1/3}$ and $\phi_h \propto (-\zeta)^{-1/3}$) for $-\zeta \gg 1$. In summary, these results provide evidence of the connection between uniform momentum and temperature zones with interfacial velocity and temperature jumps (Δu and $\Delta\theta$) across regions of thickness δ_ω and $\delta_{\nabla\theta}$ contributing to the observed scaling behaviour of the ASL mean velocity and temperature gradients following MOST.

3.6. *Conditionally averaged profiles*

In this section we consider the relationship between turbulent fluxes (viewed through the lens of quadrant analysis), UMZs and UTZs using conditional averaging. Previous work in turbulent boundary layers (e.g. Eisma *et al.* 2015; de Silva *et al.* 2017; Chen, Chung & Wan 2021) has revealed that sharp changes occur in both streamwise and wall-normal momentum across UMZ interfaces, such that ejections of momentum (Q2, where $u' < 0$ and $w' > 0$) are found below the interface and sweeps of momentum (Q4, where $u' > 0$ and $w' < 0$) are found above the interface. de Silva *et al.* (2017) noted that their findings were consistent with UMZ interfaces intersecting the heads of hairpin vortices (Adrian *et al.* 2000). We here consider how this picture is influenced by unstable stratification, examining conditionally averaged u, w, and θ profiles across both UMZ and UTZ interfaces.

Figure 13 presents conditionally averaged velocity and temperature profiles, e.g. $(\overline{u - u_{i,m}})/u_\tau$ where $u_{i,m}$ is the streamwise velocity component at the UMZ interface. Profiles are plotted in a local coordinate system as a function of $(z - z_{i,m})/\delta$, where $z_{i,m}$ is the wall-normal distance to a UMZ interface, at several selected stabilities ($-\delta/L =$ 0.3, 9.2, 261), and in bins of z/δ. Note that UMZ and UTZ interfaces at heights lower than $z/\delta = 0.05$ were omitted from averaging for the lowest bin to ensure that a sufficient number of points above the ground were available to include in conditional averages and to avoid results being influenced by the LES wall model. Lower in the boundary layer, the region below the UMZ interface is, in an average sense, characterized by negative streamwise velocity fluctuations ($u' < 0$), positive vertical velocity fluctuations ($w' > 0$) and positive temperature fluctuations ($\theta' > 0$), while region above the UMZ interface corresponds to $u' > 0$, $w' < 0$, and $\theta' < 0$. From the perspective of quadrant analysis, this corresponds to ejections of momentum (Q2) and warm updrafts (Q1, $w' > 0$ and $\theta' > 0$) below the interface, and sweeps of momentum (Q4) and cold downdrafts (Q3, $w' < 0$ and $\theta' < 0$) above the interface.

For the weakly stable ($-\delta/L = 0.3$) case, the conditionally averaged temperature gradient changes sign as z/δ increases, consistent with the deep entrainment zone (beginning around $z/\delta = 0.4$) that can be seen in figure 4(*d*). For the $-\delta/L = 9.2$ and 261 cases, higher in the boundary layer (e.g. $z/\delta = 0.5$) the conditionally averaged streamwise velocity and temperature profiles become nearly constant with height. Recall that in the

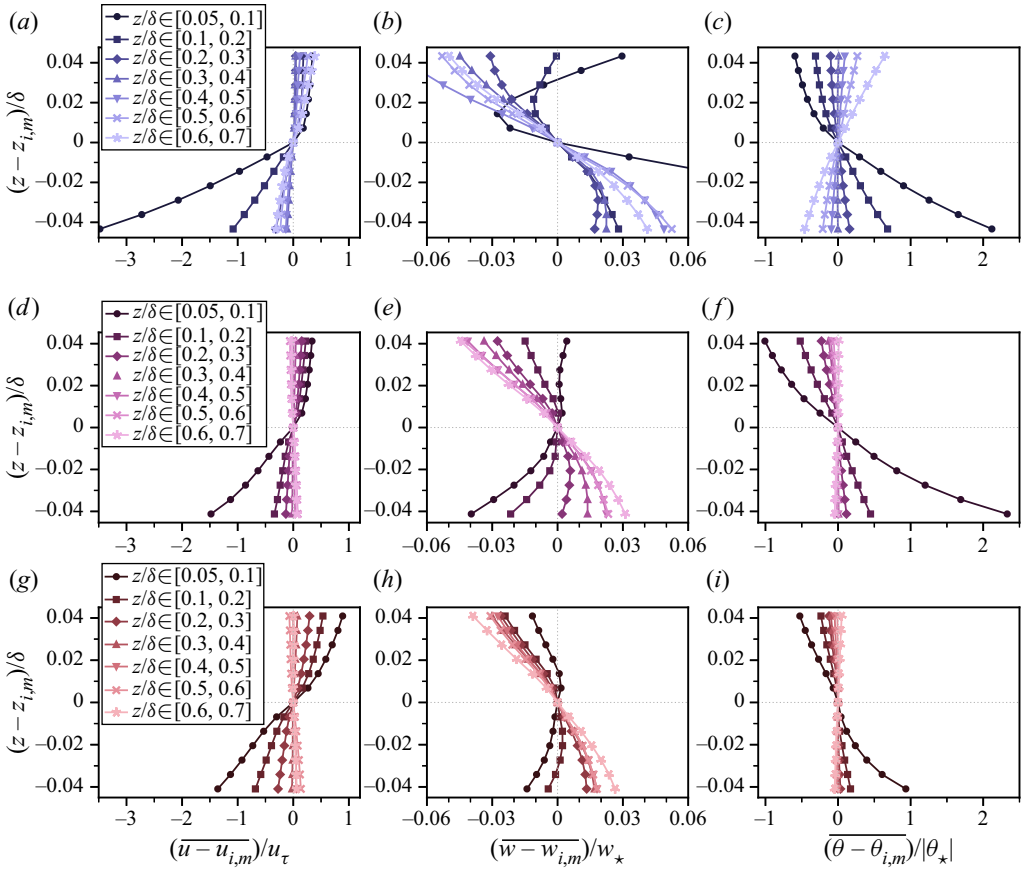

Figure 13. Conditionally averaged velocity and temperature profiles across UMZ interfaces; (*a–c*) $-\delta/L = 0.30$, (*d–f*) $-\delta/L = 9.2$, (*g–i*) $-\delta/L = 261$. (*a*,*d*,*g*) Conditionally averaged streamwise velocity $(\overline{u - u_{i,m}})/u_\tau$; (*b*,*e*,*h*) conditionally averaged wall-normal velocity $(\overline{w - w_{i,m}})/w_\star$; (*c*,*f*,*i*) conditionally averaged potential temperature $(\overline{\theta - \theta_{i,m}})/|\theta_\star|$. Profiles are displayed in a coordinate system local to UMZ interfaces, i.e. as a function of $(z - z_{i,m})/\delta$, where $z_{i,m}$ is the height of the UMZ interface. Each curve is plotted for UMZ interfaces lying within the range of z/δ values indicated in the legend.

mixed layer, $\Delta u \to 0$, and the velocity jumps have a bimodal distribution with both positive and negative peaks (figure 9*i–l*). Thus although instantaneous velocity jumps across UMZ interfaces may be either positive or negative, the conditionally averaged profiles tend towards zero.

A plot of conditional averages relative to the UTZ interfaces is presented in figure 14. Here, we observe the conditionally averaged velocity and temperature profiles across the UTZ interfaces are very similar to what is found for the UMZ interfaces. In the surface layer, ejections of momentum (Q2) and warm updrafts (Q1) occur below UTZ interfaces while sweeps of momentum (Q4) and cold downdrafts (Q3) are found above the UTZ interfaces. Higher in the boundary layer, the conditionally averaged streamwise velocity and temperature profiles tend toward zero, particularly for the $-\delta/L = 9.2$ and 261 cases. Again, these results are consistent with mean UTZ properties and their PDFs (figures 8, 9). Although one might expect significant differences between the conditional averages across UMZ vs UTZ interfaces, we find that both of these types of interfaces have a similar

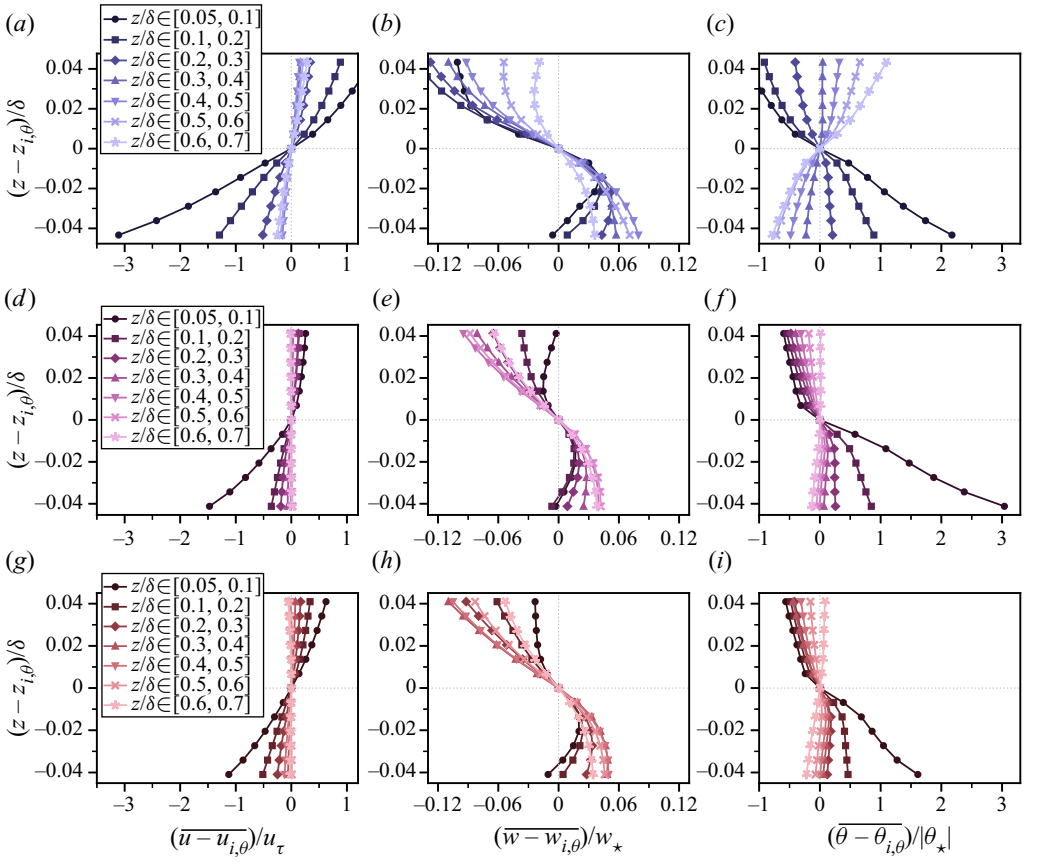

Figure 14. Conditionally averaged velocity and temperature profiles across UTZ interfaces; (*a–c*) $-\delta/L = 0.30$, (*d–f*) $-\delta/L = 9.2$, (*g–i*) $-\delta/L = 261$. (*a*,*d*,*g*) Conditionally averaged streamwise velocity $(\overline{u - u_{i,\theta}})/u_\tau$; (*b*,*e*,*h*) conditionally averaged wall-normal velocity $(\overline{w - w_{i,\theta}})/w_\star$; (*c*,*f*,*i*) conditionally averaged potential temperature $(\overline{\theta - \theta_{i,\theta}})/|\theta_\star|$. Profiles are displayed in a coordinate system local to UTZ interfaces, i.e. as a function of $(z - z_{i,m})/\delta$, where $z_{i,m}$ is the height of the UMZ interface. Each curve is plotted for UTZ interfaces lying within the range of z/δ values indicated in the legend.

association with the spatial structure of momentum and heat fluxes above and below the interface, with similar variation in the wall-normal direction and with stability.

4. Conclusions

Since the pioneering work of Meinhart & Adrian (1995), UMZs (Meinhart & Adrian 1995; Adrian *et al.* 2000; de Silva *et al.* 2016, 2017) have been an active topic of research in wall-bounded turbulent shear flows, as they have been found to be linked to the spatial structure of turbulent fluxes (de Silva *et al.* 2017; Heisel *et al.* 2018), scaling laws in the logarithmic region (Heisel *et al.* 2020) and other coherent structures in the flow (e.g. hairpin vortex packets; Adrian *et al.* 2000). Despite many advances in our understanding of UMZs in turbulent shear flows, the effects of unstable thermal stratification on UMZ structure and the extent to which temperature, an active scalar, organizes into analogous UTZs, have not been explored previously.

In the present work, we have used a suite of LES cases spanning global instability parameters ($-\delta/L$) of nearly three orders of magnitude to investigate properties of UMZs and UTZs in the convective atmospheric boundary layer. Under weakly unstable stratification, UMZs are organized as ramp-like structures inclined in the downstream direction, as found previously in neutrally stratified flows. In instantaneous flow visualizations, one large UTZ is frequently found spanning much of the convective mixed layer (e.g. $z/\delta \in [0.2, 0.8]$) with other distinct zones found in the surface layer and entrainment zone. Even larger structural differences arise between UMZs and UTZs with increasing $-\delta/L$: UTZs predominantly encompass thermal plumes, while UMZs form regions of alternating high- and low-momentum fluid due to horizontal convergence and divergence from thermally generated updrafts and downdrafts.

An examination of statistical properties of UMZs and UTZs reveals that mean zone depth for UMZs is quasi-constant with increasing wall-normal distance, while mean UTZ depth reaches its maximum value of $h_\theta/\delta = 0.15$–0.20 in the centre of the mixed layer ($z/\delta = 0.4$–0.5) for all stabilities considered herein. Interfacial average velocity jumps across UMZ interfaces were found to be $\Delta u \approx 0.5$–$1.0u_\tau$ near the ground, decreasing with height to become smaller in the mixed layer. The p.d.f.s of interfacial velocity jumps and instantaneous profiles reveal that in the mixed layer, instantaneous velocity follows alternating positive and negative jumps across UMZ interfaces with increasing height. Interfacial temperature jumps were found to be $\Delta\theta \approx -1.0\theta_\tau$ near the ground, and change sign at a height that roughly corresponds to the bottom of the entrainment zone (where $\overline{w'\theta'} < 0$). The observed mean structure of the convective mixed layer, with well-mixed temperature and velocity profiles can be viewed as a consequence of UMZs and UTZs, given the alternating positive and negative temperature jumps in this region (which are small or near zero in an ensemble mean sense).

Connections between UMZ and UTZ properties and scaling laws for the mean velocity and temperature gradients in the surface layer were examined in the context of MOST. When normalized by the friction velocity and stability-dependent mixing length for momentum, the velocity gradient based on UMZ interfacial velocity jumps and vorticity thickness ($\Delta u/\delta_\omega$) exhibits good collapse the surface layer for all stabilities, establishing a link between UMZ structure and scaling of the mean velocity gradient following MOST under unstably stratified conditions. A corresponding analysis for temperature demonstrates a clear connection between UTZ interfacial temperature jumps ($\Delta\theta$) and temperature gradient thickness ($\delta_{\nabla\theta}$) and the surface-layer scaling for $\partial\bar{\theta}/\partial z$ predicted by MOST. Conditionally averaged profiles across UMZ and UTZ interfaces indicate that in the surface layer these interfaces are associated with ejections of momentum and warm updrafts below the interface and sweeps of momentum and cool downdrafts below the interface. Our results reveal that uniform momentum and temperature zones in these unstably stratified flows are closely linked to mean boundary layer structure, instantaneous turbulent fluxes and scaling laws for the mean velocity and temperature profiles in the ASL.

Acknowledgements. The author thanks the four anonymous reviewers for their thoughtful and constructive feedback on this manuscript.

Funding. This work was supported by the US Department of Energy Atmospheric System Research Program, grant no. DE-SC0022124.

Declaration of interests. The author reports no conflict of interest.

Author ORCIDs.
Scott T. Salesky https://orcid.org/0000-0003-3291-2664.

Appendix A

In this article, we employ the empirical forms of the universal functions $\phi_m(\zeta)$ and $\phi_h(\zeta)$ presented in Brutsaert (1999). These functions are smooth interpolants of the scaling regimes presented in Kader & Yaglom (1990), who supposed that the convective ASL can be subdivided into three distinct sublayers (dynamic, dynamic-convective and free-convective) and obtained scaling laws for each via directional dimensional analysis. Specifically, Kader & Yaglom (1990) showed their data were well described by the following functions:

$$\phi_m(\zeta) = \begin{cases} 1.04, & -0.04 \leqslant \zeta \leqslant 0 \\ 0.501(-\zeta)^{-1/3}, & -1.2 \leqslant \zeta \leqslant -0.12 \\ 0.380(-\zeta)^{1/3}, & \zeta \leqslant -2 \end{cases} \tag{A1}$$

$$\phi_h(\zeta) = \begin{cases} 0.96, & -0.04 \leqslant \zeta \leqslant 0 \\ 0.324(-\zeta)^{-1/3}, & -1.2 \leqslant \zeta \leqslant -0.12 \\ 0.265(-\zeta)^{-1/3}, & \zeta \leqslant -2 \end{cases}. \tag{A2}$$

These empirical functions capture near-neutral and local free convective scaling behaviour (e.g. Wyngaard 2010) $\phi_m \propto (-\zeta)^{1/3}$ and $\phi_h \propto (-\zeta)^{-1/3}$ for $-\zeta \gg 1$, whereas other commonly used empirical functions such as the Businger-Dyer curves (Businger *et al.* 1971) are typically only considered to be valid for $-2 \leqslant \zeta \leqslant 0$. The interpolation formulas presented by Brutsaert (1999) are given as

$$\phi_m(\zeta) = \frac{a + b(-\zeta)^{m+1/3}}{a + (-\zeta)^m} \tag{A3}$$

$$\phi_h(\zeta) = \frac{c + d(-\zeta)^n}{c + (-\zeta)^n}, \tag{A4}$$

with the constants $a = 0.33$, $b = 0.41$, $m = 1.0$, $c = 0.33$, $d = 0.057$, and $n = 0.78$.

References

Adrian, R.J. 2007 Hairpin vortex organization in wall turbulence. *Phys. Fluids* **19** (4), 041301.

Adrian, R.J., Meinhart, C.D. & Tomkins, C.D. 2000 Vortex organization in the outer region of the turbulent boundary layer. *J. Fluid Mech.* **422**, 1–54.

Albertson, J.D. & Parlange, M.B. 1999 Surface length scales and shear stress: implications for land-atmosphere interaction over complex terrain. *Water Resour. Res.* **35** (7), 2121–2132.

Anderson, W. & Salesky, S.T. 2021 Uniform momentum zone scaling arguments from direct numerical simulation of inertia-dominated channel turbulence. *J. Fluid Mech.* **906**, A8.

Balakumar, B.J. & Adrian, R.J. 2007 Large-and very-large-scale motions in channel and boundary-layer flows. *Phil. Trans. R. Soc. Lond.* A **365** (1852), 665–681.

Bautista, J.C.C., Ebadi, A., White, C.M., Chini, G.P. & Klewicki, J.C. 2019 A uniform momentum zone–vortical fissure model of the turbulent boundary layer. *J. Fluid Mech.* **858**, 609–633.

Bou-Zeid, E., Meneveau, C. & Parlange, M. 2005 A scale-dependent Lagrangian dynamic model for large eddy simulation of complex turbulent flows. *Phys. Fluids* **17** (2), 025105.

Brown, G.L. & Roshko, A. 1974 On density effects and large structure in turbulent mixing layers. *J. Fluid Mech.* **64** (4), 775–816.

Brown, G.L. & Thomas, A.S.W. 1977 Large structure in a turbulent boundary layer. *Phys. Fluids* **20** (10), S243–S252.

Brutsaert, W. 1999 Aspects of bulk atmospheric boundary layer similarity under free-convective conditions. *Rev. Geophys.* **37** (4), 439–451.

Businger, J.A., Wyngaard, J.C., Izumi, Y. & Bradley, E.F. 1971 Flux-profile relationships in the atmospheric surface layer. *J. Atmos. Sci.* **28** (2), 181–189.

CANTWELL, B.J. 1981 Organized motion in turbulent flow. *Annu. Rev. Fluid Mech.* **13**, 457–515.
CANUTO, C., HUSSAINI, M.Y., QUARTERONI, A. & ZANG, T.A. 2012 *Spectral Methods in Fluid Dynamics*. Springer.
CARPER, M.A. & PORTÉ-AGEL, F. 2004 The role of coherent structures in subfilter-scale dissipation of turbulence measured in the atmospheric surface layer. *J. Turbul.* **5** (1), 040.
CHAUHAN, K., HUTCHINS, N., MONTY, J. & MARUSIC, I. 2013 Structure inclination angles in the convective atmospheric surface layer. *Boundary-Layer Meteorol.* **147** (1), 41–50.
CHAUHAN, K., PHILIP, J., DE SILVA, C.M., HUTCHINS, N. & MARUSIC, I. 2014 The turbulent/non-turbulent interface and entrainment in a boundary layer. *J. Fluid Mech.* **742**, 119–151.
CHEN, X., CHUNG, Y.M. & WAN, M. 2020 Uniform-momentum zones in a turbulent pipe flow. *J. Fluid Mech.* **884**, A25.
CHEN, X., CHUNG, Y.M. & WAN, M. 2021 The uniform-momentum zones and internal shear layers in turbulent pipe flows at Reynolds numbers up to $Re_\tau = 1000$. *Intl J. Heat Fluid Flow* **90**, 108817.
CHINI, G.P., MONTEMURO, B., WHITE, C.M. & KLEWICKI, J. 2017 A self-sustaining process model of inertial layer dynamics in high Reynolds number turbulent wall flows. *Phil. Trans. R. Soc. Lond.* A **375** (2089), 20160090.
CHORIN, A.J. 1968 Numerical solution of the Navier–Stokes equations. *Maths Comput.* **22** (104), 745–762.
CHUNG, D. & MCKEON, B.J. 2010 Large-eddy simulation of large-scale structures in long channel flow. *J. Fluid Mech.* **661**, 341–364.
CONZEMIUS, R.J. & FEDOROVICH, E. 2006 Dynamics of sheared convective boundary layer entrainment. Part I: methodological background and large-eddy simulations. *J. Atmos. Sci.* **63** (4), 1151–1178.
CORINO, E.R. & BRODKEY, R.S. 1969 A visual investigation of the wall region in turbulent flow. *J. Fluid Mech.* **37** (1), 1–30.
DEARDORFF, J.W. 1972 Numerical investigation of neutral and unstable planetary boundary layers. *J. Atmos. Sci.* **29** (1), 91–115.
DYER, A.J. 1974 A review of flux-profile relationships. *Boundary-Layer Meteorol.* **7** (3), 363–372.
EBADI, A., BAUTISTA, J.C.C., WHITE, C.M., CHINI, G. & KLEWICKI, J. 2020 A heat transfer model of fully developed turbulent channel flow. *J. Fluid Mech.* **884**, R7.
EISMA, J., WESTERWEEL, J., OOMS, G. & ELSINGA, G.E. 2015 Interfaces and internal layers in a turbulent boundary layer. *Phys. Fluids* **27** (5), 055103.
EISMA, J., WESTERWEEL, J. & VAN DE WATER, W. 2021 Do coherent structures organize scalar mixing in a turbulent boundary layer? *J. Fluid Mech.* **929**, A14.
FAN, D., XU, J., YAO, M.X. & HICKEY, J.-P. 2019 On the detection of internal interfacial layers in turbulent flows. *J. Fluid Mech.* **872**, 198–217.
FEDOROVICH, E. & CONZEMIUS, R. 2008 Effects of wind shear on the atmospheric convective boundary layer structure and evolution. *Acta Geophys.* **56** (1), 114–141.
FRENZEN, P. & VOGEL, C.A. 1992 The turbulent kinetic energy budget in the atmospheric surface layer: a review and an experimental reexamination in the field. *Boundary-Layer Meteorol.* **60** (1), 49–76.
FRENZEN, P. & VOGEL, C.A. 2001 Further studies of atmospheric turbulence in layers near the surface: scaling the TKE budget above the roughness sublayer. *Boundary-Layer Meteorol.* **99** (2), 173–206.
GANAPATHISUBRAMANI, B., LONGMIRE, E.K. & MARUSIC, I. 2003 Characteristics of vortex packets in turbulent boundary layers. *J. Fluid Mech.* **478**, 35–46.
GERMANO, M., PIOMELLI, U., MOIN, P. & CABOT, W.H. 1991 A dynamic subgrid-scale eddy viscosity model. *Phys. Fluids* A **3** (7), 1760–1765.
GUALA, M., HOMMEMA, S.E. & ADRIAN, R.J. 2006 Large-scale and very-large-scale motions in turbulent pipe flow. *J. Fluid Mech.* **554**, 521–542.
GUL, M., ELSINGA, G.E. & WESTERWEEL, J. 2020 Internal shear layers and edges of uniform momentum zones in a turbulent pipe flow. *J. Fluid Mech.* **901**, A10.
HEAD, M.R. & BANDYOPADHYAY, P. 1981 New aspects of turbulent boundary-layer structure. *J. Fluid Mech.* **107**, 297–338.
HEISEL, M., DASARI, T., LIU, Y., HONG, J., COLETTI, F. & GUALA, M. 2018 The spatial structure of the logarithmic region in very-high-Reynolds-number rough wall turbulent boundary layers. *J. Fluid Mech.* **857**, 704–747.
HEISEL, M., DE SILVA, C.M., HUTCHINS, N., MARUSIC, I. & GUALA, M. 2020 On the mixing length eddies and logarithmic mean velocity profile in wall turbulence. *J. Fluid Mech.* **887**, R1.
HEISEL, M., SULLIVAN, P.P., KATUL, G.G. & CHAMECKI, M. 2022 Turbulence organization and mean profile shapes in the stably stratified boundary layer: zones of uniform momentum and air temperature. *Boundary-Layer Meteorol.* https://doi.org/10.1007/s10546-022-00771-0.

HÖGSTRÖM, U 1988 Non-dimensional wind and temperature profiles in the atmospheric surface layer: a re-evaluation. *Boundary-Layer Meteorol.* **42** (1), 55–78.

HOMMEMA, S.E. & ADRIAN, R.J. 2003 Packet structure of surface eddies in the atmospheric boundary layer. *Boundary-Layer Meteorol.* **106** (1), 147–170.

HUTCHINS, N. & MARUSIC, I. 2007 Evidence of very long meandering features in the logarithmic region of turbulent boundary layers. *J. Fluid Mech.* **579**, 1–28.

JIMÉNEZ, J. 2018 Coherent structures in wall-bounded turbulence. *J. Fluid Mech.* **842**, P1.

JOHANSSON, C., SMEDMAN, A.-S., HÖGSTRÖM, U., BRASSEUR, J.G. & KHANNA, S. 2001 Critical test of the validity of Monin–Obukhov similarity during convective conditions. *J. Atmos. Sci.* **58** (12), 1549–1566.

KADER, B.A. & YAGLOM, A.M. 1990 Mean fields and fluctuation moments in unstably stratified turbulent boundary layers. *J. Fluid Mech.* **212**, 637–662.

KAIMAL, J.C. & FINNIGAN, J.J. 1994 *Atmospheric Boundary Layer Flows: Their Structure and Measurement*, p. 304. Oxford University Press.

KAIMAL, J.C., WYNGAARD, J.C., IZUMI, Y. & COTÉ, O.R. 1972 Spectral characteristics of surface-layer turbulence. *Q. J. R. Meteorol. Soc.* **98** (417), 563–589.

KANG, H.S. & MENEVEAU, C. 2002 Universality of large eddy simulation model parameters across a turbulent wake behind a heated cylinder. *J. Turbul.* **3** (1), 032.

KHANNA, S. & BRASSEUR, J.G. 1997 Analysis of Monin–Obukhov similarity from large-eddy simulation. *J. Fluid Mech.* **345**, 251–286.

KHANNA, S. & BRASSEUR, J.G. 1998 Three-dimensional buoyancy-and shear-induced local structure of the atmospheric boundary layer. *J. Atmos. Sci.* **55** (5), 710–743.

KIM, J. & MOIN, P. 1985 Application of a fractional-step method to incompressible Navier–Stokes equations. *J. Comput. Phys.* **59** (2), 308–323.

KIM, K.C. & ADRIAN, R.J. 1999 Very large-scale motion in the outer layer. *Phys. Fluids* **11** (2), 417–422.

KLEISSL, J., KUMAR, V., MENEVEAU, C. & PARLANGE, M.B. 2006 Numerical study of dynamic Smagorinsky models in large-eddy simulation of the atmospheric boundary layer: validation in stable and unstable conditions. *Water Resour. Res.* **42**, W06D10.

KLINE, S.J., REYNOLDS, W.C., SCHRAUB, F.A. & RUNSTADLER, P.W. 1967 The structure of turbulent boundary layers. *J. Fluid Mech.* **30** (04), 741–773.

KOVASZNAY, L.S.G., KIBENS, V. & BLACKWELDER, R.F. 1970 Large-scale motion in the intermittent region of a turbulent boundary layer. *J. Fluid Mech.* **41** (2), 283–325.

KUMAR, V., KLEISSL, J., MENEVEAU, C. & PARLANGE, M.B. 2006 Large-eddy simulation of a diurnal cycle of the atmospheric boundary layer: atmospheric stability and scaling issues. *Water Resour. Res.* **42**, W06D09.

KWON, Y.S., PHILIP, J., DE SILVA, C.M., HUTCHINS, N. & MONTY, J.P. 2014 The quiescent core of turbulent channel flow. *J. Fluid Mech.* **751**, 228–254.

LASKARI, A., DE KAT, R., HEARST, R.J. & GANAPATHISUBRAMANI, B. 2018 Time evolution of uniform momentum zones in a turbulent boundary layer. *J. Fluid Mech.* **842**, 554–590.

LI, D. & BOU-ZEID, E. 2011 Coherent structures and the dissimilarity of turbulent transport of momentum and scalars in the unstable atmospheric surface layer. *Boundary-Layer Meteorol.* **140** (2), 243–262.

MARUSIC, I. & HUTCHINS, N. 2008 Study of the log-layer structure in wall turbulence over a very large range of Reynolds number. *Flow Turbul. Combust.* **81** (1–2), 115–130.

MARUSIC, I., MCKEON, B.J., MONKEWITZ, P.A., NAGIB, H.M., SMITS, A.J. & SREENIVASAN, K.R. 2010 Wall-bounded turbulent flows at high Reynolds numbers: recent advances and key issues. *Phys. Fluids* **22** (6), 065103.

MARUSIC, I. & MONTY, J.P. 2019 Attached eddy model of wall turbulence. *Annu. Rev. Fluid Mech.* **51**, 49–74.

MATHIS, R., HUTCHINS, N. & MARUSIC, I. 2009 Large-scale amplitude modulation of the small-scale structures in turbulent boundary layers. *J. Fluid Mech.* **628**, 311–337.

MEINHART, C.D. & ADRIAN, R.J. 1995 On the existence of uniform momentum zones in a turbulent boundary layer. *Phys. Fluids* **7** (4), 694–696.

MENEVEAU, C., LUND, T.S. & CABOT, W.H. 1996 A Lagrangian dynamic subgrid-scale model of turbulence. *J. Fluid Mech.* **319**, 353–385.

MOENG, C.-H. & SULLIVAN, P.P. 1994 A comparison of shear-and buoyancy-driven planetary boundary layer flows. *J. Atmos. Sci.* **51** (7), 999–1022.

MONIN, A.S. & OBUKHOV, A.M. 1954 Turbulent mixing in the atmospheric surface layer. *Tr. Akad. Nauk SSSR Geofiz. Inst.* **24** (151), 163–187.

MONIN, A.S. & YAGLOM, A.M. 2007*a* *Statistical Fluid Mechanics, Volume I: Mechanics of Turbulence*, vol. 1. Dover.

MONIN, A.S. & YAGLOM, A.M. 2007*b* *Statistical Fluid Mechanics, Volume II: Mechanics of Turbulence*, vol. 2. Dover.

MONTEMURO, B., WHITE, C.M., KLEWICKI, J.C. & CHINI, G.P. 2020 A self-sustaining process theory for uniform momentum zones and internal shear layers in high Reynolds number shear flows. *J. Fluid Mech.* **901**, A28.

MORRIS, S.C., STOLPA, S.R., SLABOCH, P.E. & KLEWICKI, J.C. 2007 Near-surface particle image velocimetry measurements in a transitionally rough-wall atmospheric boundary layer. *J. Fluid Mech.* **580**, 319–338.

NIEUWSTADT, F.T.M., MASON, P.J., MOENG, C.-H. & SCHUMANN, U. 1993 Large-eddy simulation of the convective boundary layer: a comparison of four computer codes. In *Turbulent Shear Flows* (ed. F. Durst, R. Friedrich, B.E. Launder, F.W. Schmidt, U. Schumann & J.H. Whitelaw), vol. 8, pp. 343–367. Springer.

OBUKHOV, A.M. 1946 Turbulence in an atmosphere with temperature inhomogeneities. *Tr. Inst. Theor. Geofiz.* **1**, 95–115.

OFFEN, G.R. & KLINE, S.J. 1974 Combined dye-streak and hydrogen-bubble visual observations of a turbulent boundary layer. *J. Fluid Mech.* **62** (2), 223–239.

OFFEN, G.R. & KLINE, S.J. 1975 A proposed model of the bursting process in turbulent boundary layers. *J. Fluid Mech.* **70** (2), 209–228.

PANTON, R.L. 2001 Overview of the self-sustaining mechanisms of wall turbulence. *Prog. Aerosp. Sci.* **37** (4), 341–383.

PATTON, E.G., SULLIVAN, P.P., SHAW, R.H., FINNIGAN, J.J. & WEIL, J.C. 2016 Atmospheric stability influences on coupled boundary layer and canopy turbulence. *J. Atmos. Sci.* **73** (4), 1621–1647.

PERRY, A.E. & CHONG, M.S. 1982 On the mechanism of wall turbulence. *J. Fluid Mech.* **119**, 173–217.

PERRY, A.E., HENBEST, S. & CHONG, M.S. 1986 A theoretical and experimental study of wall turbulence. *J. Fluid Mech.* **165**, 163–199.

PERRY, A.E. & MARUSIC, I. 1995 A wall-wake model for the turbulence structure of boundary layers. Part 1. Extension of the attached eddy hypothesis. *J. Fluid Mech.* **298**, 361–388.

POPE, S.B. 2000 *Turbulent Flows*, p. 802. Cambridge University Press.

PORTÉ-AGEL, F. 2004 A scale-dependent dynamic model for scalar transport in large-eddy simulations of the atmospheric boundary layer. *Boundary-Layer Meteorol.* **112** (1), 81–105.

PRANDTL, L. 1925 Bericht über untersuchungen zur ausgebildeten turbulenz. *Z. Angew. Math. Mech.* **5**, 136–139.

ROBINSON, S.K. 1991 Coherent motions in the turbulent boundary layer. *Annu. Rev. Fluid Mech.* **23** (1), 601–639.

SALESKY, S.T. & ANDERSON, W. 2018 Buoyancy effects on large-scale motions in convective atmospheric boundary layers: implications for modulation of near-wall processes. *J. Fluid Mech.* **856**, 135–168.

SALESKY, S.T. & ANDERSON, W. 2020*a* Coherent structures modulate atmospheric surface layer flux-gradient relationships. *Phys. Rev. Lett.* **125** (12), 124501.

SALESKY, S.T. & ANDERSON, W. 2020*b* Revisiting inclination of large-scale motions in unstably stratified channel flow. *J. Fluid Mech.* **884**, R5.

SALESKY, S.T. & CHAMECKI, M. 2012 Random errors in turbulence measurements in the atmospheric surface layer: implications for Monin–Obukhov similarity theory. *J. Atmos. Sci.* **69** (12), 3700–3714.

SALESKY, S.T., CHAMECKI, M. & BOU-ZEID, E. 2017 On the nature of the transition between roll and cellular organization in the convective boundary layer. *Boundary-Layer Meteorol.* **163** (1), 41–68.

SALESKY, S.T., KATUL, G.G. & CHAMECKI, M. 2013 Buoyancy effects on the integral lengthscales and mean velocity profile in atmospheric surface layer flows. *Phys. Fluids* **25** (10), 105101.

SCHMIDT, H. & SCHUMANN, U. 1989 Coherent structure of the convective boundary layer derived from large-eddy simulations. *J. Fluid Mech.* **200**, 511–562.

DE SILVA, C.M., HUTCHINS, N. & MARUSIC, I. 2016 Uniform momentum zones in turbulent boundary layers. *J. Fluid Mech.* **786**, 309–331.

DE SILVA, C.M., PHILIP, J., HUTCHINS, N. & MARUSIC, I. 2017 Interfaces of uniform momentum zones in turbulent boundary layers. *J. Fluid Mech.* **820**, 451–478.

STOLL, R. & PORTÉ-AGEL, F. 2006 Dynamic subgrid-scale models for momentum and scalar fluxes in large-eddy simulations of neutrally stratified atmospheric boundary layers over heterogeneous terrain. *Water Resour. Res.* **42**, W01409.

SULLIVAN, P.P., HORST, T.W., LENSCHOW, D.H., MOENG, C.-H. & WEIL, J.C. 2003 Structure of subfilter-scale fluxes in the atmospheric surface layer with application to large-eddy simulation modelling. *J. Fluid Mech.* **482**, 101–139.

SULLIVAN, P.P. & PATTON, E.G. 2011 The effect of mesh resolution on convective boundary layer statistics and structures generated by large-eddy simulation. *J. Atmos. Sci.* **68** (10), 2395–2415.

THEODORSEN, T. 1952 Mechanism of turbulence. In *Proceedings of the Second Midwestern Conference on Fluid Mechanics* (ed. R.W. Powell, S.M. Marco & A.N. Tifford), vol. 1719. Ohio State University.

TOWNSEND, A.A. 1976 *The Structure of Turbulent Shear Flow*. Cambridge University Press.

WALLACE, J.M., ECKELMANN, H. & BRODKEY, R.S. 1972 The wall region in turbulent shear flow. *J. Fluid Mech.* **54** (1), 39–48.

WARHAFT, Z. 2000 Passive scalars in turbulent flows. *Annu. Rev. Fluid Mech.* **32** (1), 203–240.

WILLMARTH, W.W. & LU, S.S. 1972 Structure of the Reynolds stress near the wall. *J. Fluid Mech.* **55** (1), 65–92.

WOODCOCK, J.D. & MARUSIC, I. 2015 The statistical behaviour of attached eddies. *Phys. Fluids* **27** (1), 015104.

WYNGAARD, J.C. & COTÉ, O.R. 1971 The budgets of turbulent kinetic energy and temperature variance in the atmospheric surface layer. *J. Atmos. Sci.* **28** (2), 190–201.

WYNGAARD, J.C. 2010 *Turbulence in the Atmosphere*. Cambridge University Press.

YAO, M.X., SUN, Z., SCALO, C. & HICKEY, J.-P. 2019 Vortical and thermal interfacial layers in wall-bounded turbulent flows under transcritical conditions. *Phys. Rev. Fluids* **4** (8), 084604.

ZHENG, Y. & ANDERSON, W. 2022 Evidence that uniform momentum zones originate from roughness sublayer structure interactions in fully rough channel turbulence. *J. Fluid Mech.* **944**, A33.